(2)

DOCUMENTATION PAGE

Form Approved
OMB No. 0704-0188

1. AGENCY USE ONLY (Leave blank)	2. REPORT DATE	3. REPORT TYPE AND DATES COVERED
	10 November 92	Final Tech. 15 Nov 89-29 Jun 92

4. TITLE AND SUBTITLE
Rate and Confinement Effects on Cracking and Failure in Uniaxial Compression of Concrete

5. FUNDING NUMBERS
C AFOSR-90-0074

6. AUTHOR(S)
Lawrence E. Malvern
David A. Jenkins
Robert T. DeHoff

AFOSR-TR- 93 0071

7. PERFORMING ORGANIZATION NAME(S) AND ADDRESS(ES)
Dept. of Aerospace Engineering, Mechanics and Engineering Science, 231 Aero Bldg., University of Florida, Gainesville, FL 32611-2031

8. PERFORMING ORGANIZATION REPORT NUMBER

9. SPONSORING/MONITORING AGENCY NAME(S) AND ADDRESS(ES)
Air Force Office of Scientific Research, AFOSR/NA
Building 410
Bolling AFB, DC 20332-6448

10. SPONSORING/MONITORING AGENCY REPORT NUMBER

11. SUPPLEMENTARY NOTES

12a. DISTRIBUTION/AVAILABILITY STATEMENT
UNLIMITED

12b. DISTRIBUTION CODE

13. ABSTRACT (Maximum 200 words)

Crack patterns on longitudinal sections of specimens subjected to quasistatic and high-rate uniaxial compression, interrupted after various levels of maximum strain, so that intact specimens could be recovered, were examined. Damaged specimens were stabilized by an infiltrant containing a fluorescent dye to make the cracks stand out clearly under ultraviolet light, facilitating automated image analysis. Macroscopic cracking began near the lateral surface at maximum strains less than the peak-stress critical strain, and spread inward.

The image analysis showed that total crack length, number of branch points, and number of end points, each reckoned per unit area, all increase roughly linearly with strain with dynamic values significantly higher than static values at each level of maximum strain. When branch and end point counts were plotted against crack length per unit area, however, the static and dynamic plots coincided, showing that the crack pattern structure was determined by the microstructure of the medium, while all the rate dependence of the mechanical response was a result of the rate dependence of the evolution of a crack density parameter related to the crack length per unit area.

14. SUBJECT TERMS	15. NUMBER OF PAGES
Concrete, Rate Effects, Damage, Cracking, Compressive Tests, Petrographic Examination, Stereology, Automated Image Analysis, Failure	85
	16. PRICE CODE

17. SECURITY CLASSIFICATION OF REPORT	18. SECURITY CLASSIFICATION OF THIS PAGE	19. SECURITY CLASSIFICATION OF ABSTRACT	20. LIMITATION OF ABSTRACT
UNCLASSIFIED	UNCLASSIFIED	UNCLASSIFIED	UL

NSN 7540-01-280-5500

Standard Form 298 (Rev. 2-89)
Prescribed by ANSI Std. Z39-18
298-102

RATE AND CONFINEMENT EFFECTS ON CRACKING AND FAILURE IN UNIAXIAL COMPRESSION OF CONCRETE

FINAL REPORT

LAWRENCE E. MALVERN

DAVID A. JENKINS

DEPARTMENT OF AEROSPACE ENGINEERING,
MECHANICS AND ENGINEERING SCIENCE

ROBERT T. DEHOFF
DEPARTMENT OF MATERIALS SCIENCE AND ENGINEERING

UNIVERSITY OF FLORIDA
GAINESVILLE, FLORIDA 32611

10 NOVEMBER 1992

U.S. AIR FORCE OFFICE OF SCIENTIFIC RESEARCH

CONTRACT NUMBER AFOSR-90-0074

UNIVERSITY OF FLORIDA

PREFACE

This is the final technical report on a research program sponsored by the U.S. Air Force Office of Scientific Research, Directorate of Aerospace Sciences, Bldg. 410, Bolling Air Force Base, D.C. 20332-6448. Program Manager for the Air Force is Dr. Spencer Wu. This final report describes the technical effort during the period from 15 November 1989 through 29 June 1992.

The contractor is the University of Florida, Division of Sponsored Research, 219 Grinter Hall, Gainesville, Florida 32611. The research was performed by personnel of the Department of Aerospace Engineering, Mechanics, and Engineering Sciences, and the Department of Materials Science and Engineering, University of Florida, Gainesville, Florida, 32611, at the Gainesville campus of the University. Co-Principal Investigators are Professor Lawrence E. Malvern and Dr. David A. Jenkins.

TABLE OF CONTENTS

(continued)

TABLE OF CONTENTS (continued)

LIST OF FIGURES

(CONTINUED)

LIST OF FIGURES (CONTINUED)

LIST OF TABLES

Table

APPENDIX TABLES

SECTION I
INTRODUCTION

1.1 Overview

This research program was proposed to determine how the crack density and crack pattern are related to the amount of deformation, the rate of deformation, and the amount of lateral confinement in compression testing of concrete in a Split Hopkinson Pressure Bar (SHPB) system. The objective was to explain the observed rate effects in concrete in terms of the crack initiation and growth. The ultimate goal is to use the results as a basis for a rational approach to constitutive modeling. All these issues were addressed in the experimental program described in this report, except for the effect of lateral confinement of the compression specimens.

A method of interrupting unconfined tests by means of a loosely fitting steel collar around the specimen permits intact specimens, from regimes both before and after the peak stress, to be recovered for sectioning and micrographic examination. After each test the intact specimen is vacuum infiltrated with a monomer, which is polymerized to stabilize the specimen for sectioning and polishing. To make the cracks stand out clearly, a fluorescein dye is added to the infiltrant, and the sections are photographed under ultraviolet light for subsequent automated image analysis of the crack pattern.

The automated image analysis of the crack patterns showed that such characteristics of the crack patterns as the total crack length, number of branch points and number of end points, each reckoned per unit area of the section examined, each increase approximately linearly with the maximum strain reached in the interrupted tests with dynamic values being significantly higher than static values at corresponding levels of maximum strain.

The most significant results appeared when the branch and end point counts were plotted against crack length per unit area. **Static and dynamic plots then coincided**, showing that the crack pattern structure was determined by the microstructure of the medium, while the rate dependence in the mechanical results was all

a result of the rate dependence of the evolution of a crack density parameter related to the crack length per unit area. [In the mechanical results, the dynamic strengths were up to 1.8 times the static strengths.]

1.2 Background

This procedure for interrupting the SHPB compression tests by use of a collar around the specimen was devised in a preliminary investigation completed in 1988, References 1 and 2. A detailed literature survey on dynamic testing not interrupted by a collar was published in a 1986 paper, Reference 3, which also presented results obtained up to that time on high-strength concrete specimens in the SHPB system at the University of Florida. Additional uninterrupted SHPB compressive test results on concrete, obtained at the University of Florida, were reported in References 4-12. An earlier paper gave some results on mortar in a smaller SHPB system, Reference 13. References 7-11 included compression tests of laterally confined concrete.

1.3 Scope of this Report

Mechanical test procedures and results are described in Section II, including both quasistatic tests and dynamic SHPB tests, interrupted by a collar to facilitate recovery of intact specimens for examination. A few uninterrupted tests are also included for comparison.

Section III describes procedures and results of crack pattern observation, especially the quantitative stereological procedures of automated image analysis which furnish the major contribution of this investigation. Some damage-based constitutive models are reviewed in Section IV, which concludes with a discussion of the relevance of our experimental results to the hypotheses of the models.

Conclusions and recommendations for further research are then given in Section V.

SECTION II
MECHANICAL TESTS

2.1 Introduction

Mechanical test procedures are described in Section 2.2, beginning in Section 2.2.1 with procedures for preparation of the specimens used in both quasistatic and dynamic tests. This is followed by a Section 2.2.2 describing the procedures of dynamic testing with the Split Hopkinson Bar. Mechanical test results, both static and dynamic, are summarized in Section 2.3.

2.2 Test Procedures

2.2.1 Specimen Preparation

The concrete mixes for all the specimens used for au[illegible]d image analysis were based on Calera limestone for both t[illegible] aggregate and the coarse aggregate. The reason for this cho[illegible]s that the Calera limestone is opaque and not naturally fluorescent. During the first year of this program an attempt was made to use a conventional sand for the fine aggregate and Calera limestone for the coarse aggregate. The recovered specimens were infiltrated with a monomer containing a fluorescein dye and, after curing, were sectioned and polished. The polished sections, examined under ultraviolet light, showed brightly contrasting cracks against a dark background for cracks through the coarse aggregate particles, but a more diffuse bright region for cracks in the mortar. The transparent sand particles allowed light reflected from the fluorescein dye in cracks beneath the sand particles to shine through and confuse the pattern, so that automated image analysis was impossible.

To prepare the fine aggregate, a quantity of Calera limestone was carefully ground and graded by sieve analysis. The aggregate proportions listed in Table A-1 of Appendix A were used for all batches of concrete prepared for both static and dynamic tests. Specific concrete mixes for the two batches of specimens prepared are given in Table A-2 of Appendix A.

Batch B specimens had a slightly higher water content than Batch A, but were otherwise the same.

Specimen blanks were cast in two-inch-diameter split molds. After removal from the molds the following day, the blanks were stored in a misting room for two weeks, after which they were kept moist to prevent cracking and were cut to approximate lengths with a diamond saw. Each specimen was then ground to the desired length in a special fixture that ensured parallelism of the ends. All the dynamic tests of each of the basic Series A and Series B tests were completed within a few days, beginning about a month after the casting of that batch of specimens. The static tests of both Series A and Series B were performed in one day, about two months after the casting. Some of the specimens from Batch A were not tested in the basic Series A, but were used about a year later, as will be explained in Section 2.3.2.

2.2.2 High-Strain-Rate Testing with the Split Hopkinson Pressure Bar (SHPB) System

The SHPB system consists of two long 3-inch-diameter (76.2 mm) strain-gaged pressure bars, the incident or input bar and the transmitter bar, with a short specimen sandwiched between them. Analysis of the observed incident and reflected longitudinal elastic strain-wave pulses in the incident bar and the transmitted pulse in the transmitter bar furnishes information about both the bar force and end displacement versus time at each of the two specimen interfaces. From this record the average stress and strain in the specimen are deduced. This facility is the only one of its size in the United States.

As currently configured it provides a loading pulse lasting 300 microseconds, imparted by impact of the 30-inch (762 mm) striker bar against the incident pressure bar. The whole system, including gas gun, pressure bars and a shock absorber at the far end, is almost 30 feet (9.15 m) long.

For purposes of analysis, the three recorded pressure-bar pulses are time-shifted, so that time zero coincides with the

arrival at the first specimen interface, and corrected for wave dispersion in the pressure bars, using a procedure developed under Task Order 85-6 from AFESC/RDC, Tyndall AFB, Florida, References 6 and 14. The dispersion-correction procedure is similar to that used by Follansbee and Frantz, Reference 15, and Felice, Reference 16, except that it uses a more efficient Fast Fourier Transform method instead of a Fourier series.

Although the corrected and uncorrected pulses appear similar, the differences in detail, especially for the incident and reflected pulses (which are added algebraically to obtain the pressure bar strain at the first specimen interface) lead to significant differences in the first interface stresses. The dispersion correction leads to much closer agreement of the two interface stresses, with approximate equality of the two stresses by the time they have reached half the maximum stress in some concrete specimens with both length and diameter equal to 3 inches, Reference 6. The dispersion correction eliminated the oscillations previously reported in the first-interface stress-time records in these tests of high-strength concrete with specimens of the same diameter as the pressure bars. The dispersion correction is not so successful when the specimen is of smaller diameter than the pressure bars, and it encounters additional difficulty when a collar is used to interrupt the tests.

Figure 1 shows the dispersion-corrected stress-time plots for the two interface stresses of a 2-inch-diameter specimen of length 1.589 inches without a collar. The solid curve is for the first interface and the dashed curve for the second. The little negative dip at the beginning is an artifact introduced by the dispersion correction. After about 45 microseconds from the time the loading pulse reached the specimen, the rising portions of the two curves are both smooth and agree fairly will until the peak stress is approached, after which the first interface record shows severe oscillations that make determination of the peak unreliable. All the specimen stress-strain curves were therefore determined as plots of the second-interface stress versus the strain.

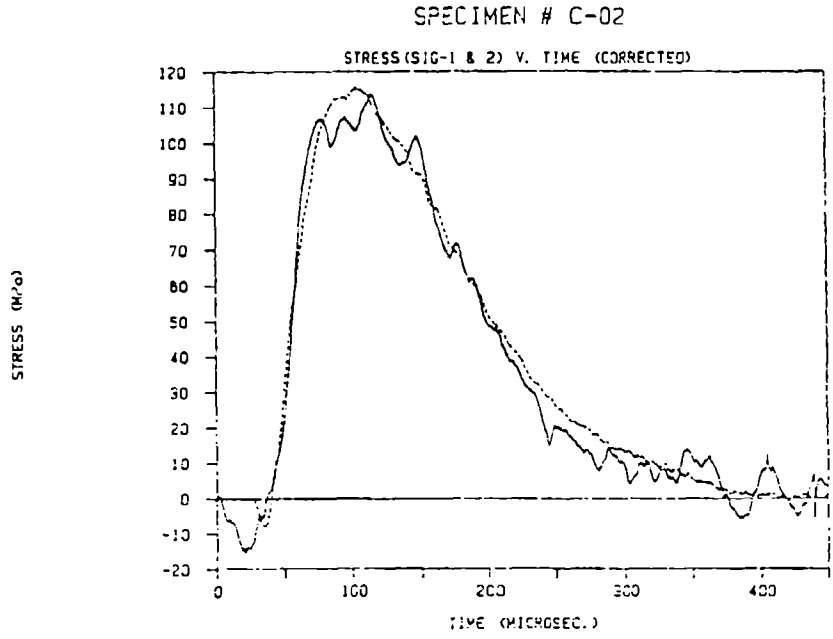

Figure 1. Stress-time curves at two interfaces of Specimen No. C-02 (dashed curve for second interface).

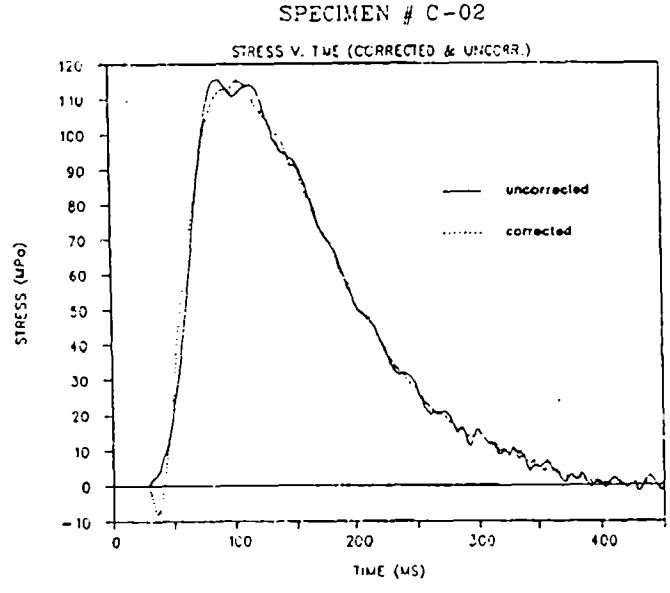

Figure 2. Dispersion-corrected and uncorrected stress-time curves for the specimen of Figure 1.

Figure 2 shows dispersion-corrected and uncorrected stress-time curves for the second interface stress of the same specimen for which the dispersion-corrected stresses at the two interfaces were shown in Figure 1. The rising portions of the two curves in Figure 2 agree quite well, except for the dip at the beginning of the corrcted curve and differences near the peak. The corrected curve is believed to be more reliable for the second-interface stress in tests that were not interrupted by the collar, but the collar introduces some irregularities in the dispersion-corrected curve, even at times before the collar begins to act, as will be shown below.

For Series A tests, the ends of the specimens were ground flat and parallel on a surface grinder to produce a series of finished lengths ranging from 1.6175 to 1.632 inches (41.1 to 41.5 mm) for subsequent static and dynamic testing. A steel collar 1.622 inches (41.2 mm) in length with a bore of 2.050 inches (52.1 mm) and an outside diameter of 3 inches (76.2 mm) was fabricated. The collar, which is shown in Figure 3, was intended to stop each static and dynamic test near the desired level of strain. It was quite successful in permitting intact specimens to be recovered for micrographic examination even in cases where the peak stress had been passed and the strain-softening regime entered before the collar began to act.

The collar is equipped with two axially mounted strain gages to indicate the time at which the collar begins to act and also to estimate the part of the axial force carried by the collar. When the collar force is subtracted from the total axial force on the transmitter bar, given by the SHPB analysis, the force carried by the specimen while the collar acts be estimated. Figure 4 is an example of the recorded collar pulse.

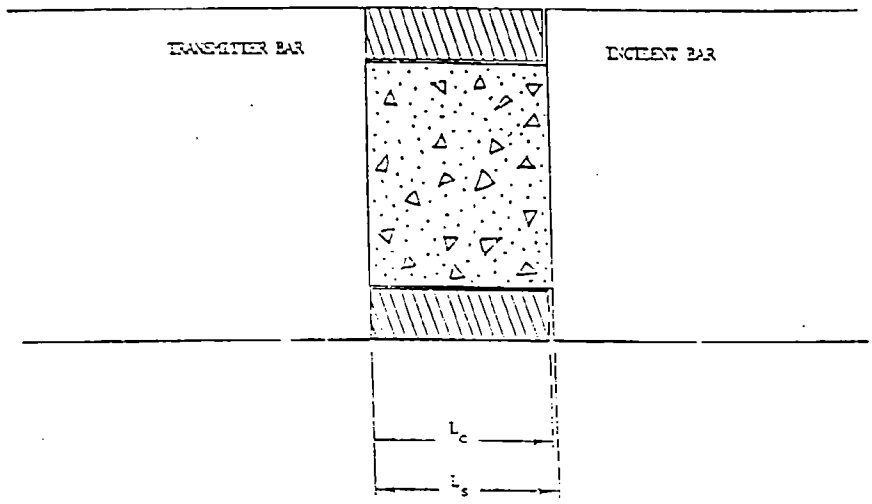

Figure 3. Specimen and collar in place before test. Specimen L_s minus collar L_c is the "overlength."

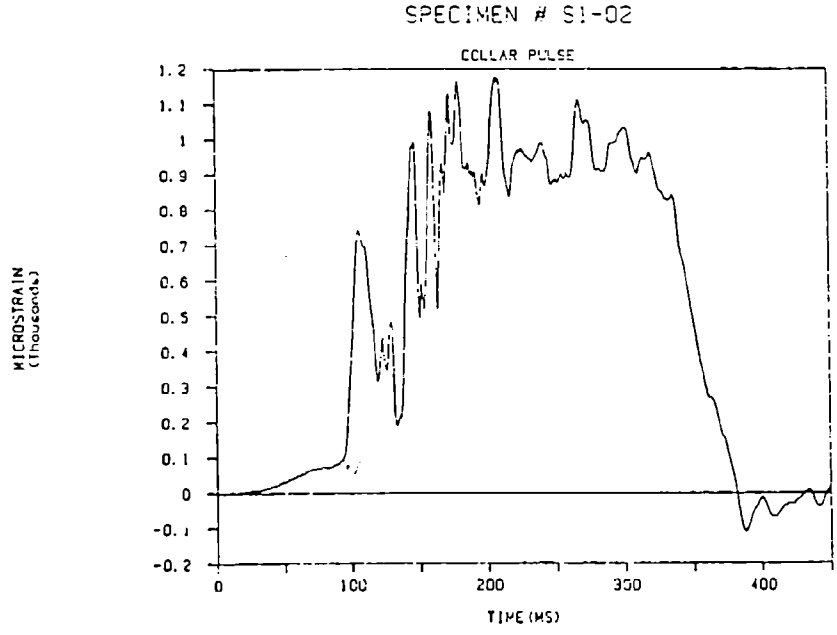

Figure 4. Example of recorded collar strain pulse.

Because of the dynamic response of the short collar to the axial impact, the axial strains, recorded at midlength on the collar, exhibit large oscillations, which make the determination of specimen stress almost impossible after the collar begins to act.

The rapid oscillations in collar force are also transmitted into the pressure bars, affecting the frequency contents of the reflected and transmitted pulses in the pressure bars, so that the dispersion correction procedure for the pressure-bar pulses leads to oscillations in the dispersion-corrected transmitted pulse, and hence in the calculated specimen stress, even at times before the collar beings to act.

Figure 5 shows an example of the calculated second-interface stress-time curve for a specimen with sufficient overlength that a peak stress was reached and the strain softening regime entered at about 80 microseconds, before the collar began to act significantly at about 90 microseconds. The recorded collar strain pulse for this specimen was given in Figure 4. Figure 5(a) was obtained without dispersion correction of the transmitter bar stress wave, while Figure 5(b) shows the results with the dispersion-corrected analysis. Neither gives a plausible measure of the specimen stress after the collar acts, but the uncorrected curve is considered more reliable up to the time of the collar action.

The uncorrected curve was used to calculate the stress-strain behavior up to the time of collar action in the results of Section 2.3.2 for those specimens where a peak stress was reached before the collar interrupted the test. Figure 6 shows the dynamic stress-strain curve for the specimen of Figure 5.

Significant collar action began at a strain of about 0.61 percent. The peak stress was 15.34 KSI (105.8 MPa). The critical strain (at peak stress) was 0.53 percent. The part of the curve after collar action began is not useful.

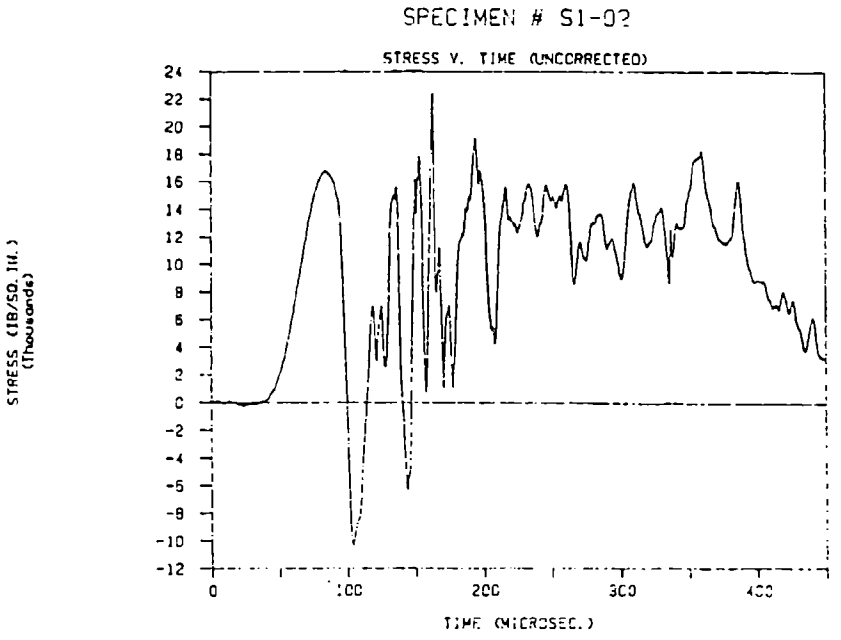

(a) without dispersion correction

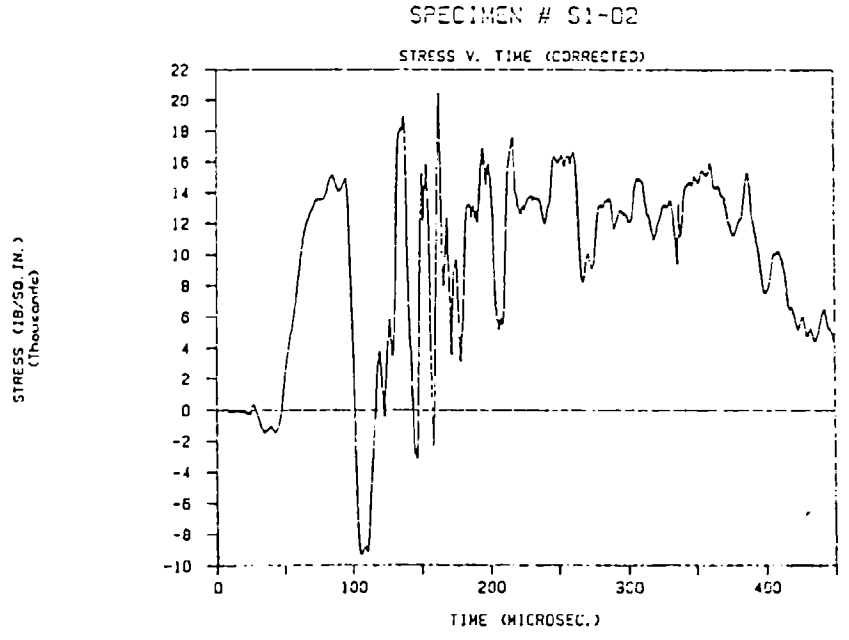

(b) with dispersion correction

Figure 5. Stress-time plots for Specimen S1-02.

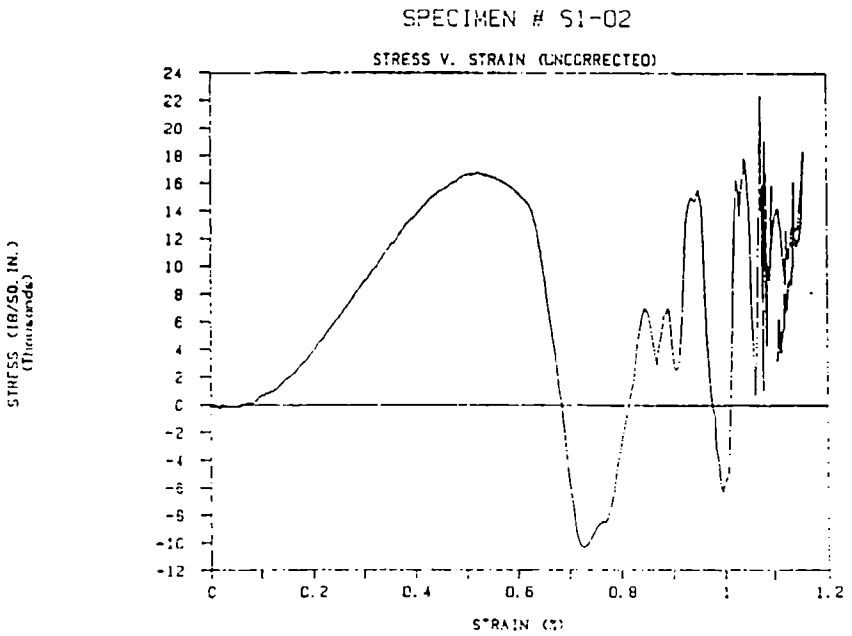

Figure 6. Dynamic stress-strain curve for Specimen S1-02.

The uncorrected transmitter-bar versus time records are considered reliable for determining the magnitude of the peak stress when the peak was reached before the collar action began, although there may be some uncertainty about the exact time (and critical strain) at which the peak stress was reached.

In static tests the output from the strain gages on the collar is quite useful for determining the occurrence of the first contact with the collar in order to stop the tests promptly. In the dynamic tests the collar is itself elastically shortened a significant amount before the closure of the pressure bars is stopped. The collar strain recorded during the dynamic tests is added to the "overlength" strain to provide an independent check to compare with the maximum axial strain of the specimen according the SHPB analysis.

2.3 Mechanical Test Results

2.3.1 Introduction

A total of 130 specimens were prepared for mechanical testing, following the procedures described in Section 2.2.1, in 2 batches, 74 in Batch A and 56 in Batch B. The sieve analysis and concrete mixes for the two batches are given in the Appendix A. Batch B had slightly higher water content than Batch A.

Two series of tests were designed to be used for crack pattern analysis. Series A, including 23 quasistatic tests and 26 dynamic tests with the SHPB, used specimens from Batch A. Series B, including 23 quasistatic tests and 28 dynamic tests, used specimens from Batch B. All the dynamic tests in each series were performed within a few days to ensure that all specimens in the series were tested in the same condition. The quasistatic tests were performed about a month later. All dynamic test mechanical results were recorded on a digital oscilloscope, and saved on diskettes for later computer analysis.

All the individual test results reported are for material from Batch A, but summarizing tables will include some results from Batch B. Since most of the dynamic mechanical tests in these two series were interrupted by the collar action before the peak stress was reached, very little information about the strength was obtained in the dynamic tests, as is reported in Section 2.3.3, which also includes results of a few mechanical tests not interrupted by a collar, for which image analysis was not performed.

2.3.2 Quasistatic Tests.

Compression tests were performed in the 50,000-lb capacity testing machine at AFCESA/RACO, Tyndall AFB, FL, at two different constant nominal strain rates. For Series A these included 14 tests at a compressive strain rate of 7.5×10^{-5} s^{-1} and 9 tests at a strain rate of 7.5×10^{-3} s^{-1}. Figure 7 shows recorded load-displacement curves for 5 of the slower rate tests, which were stopped at maximum compressive strains from 0.0022 to 0.0062. The first two were stopped before the peak stress was reached.

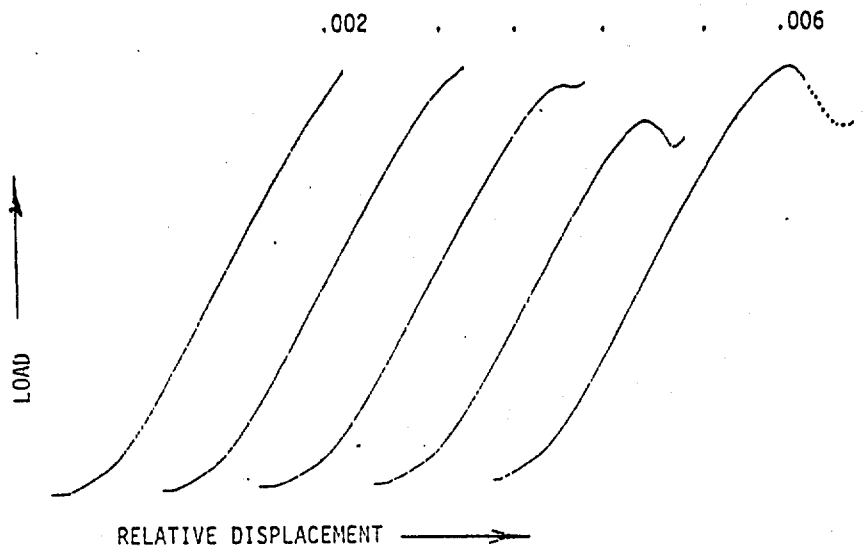

Figure 7. Load-displacement curves for five static tests.

In the last three three curves of Figure 7, a peak was reached and the strain-softening regime entered before the collar acted, so that peak stress and critical strain (at the peak stress) could be obtained. The upward turn at the end of these last 3 curves is caused by the load carried by the collar and does not signify an increase in specimen stress. Photographs of the crack patterns on sections of these 5 specimens are given in Section 3.3.

Peak stresses and critical strains were also recorded in 3 other tests at the same strain rate. The resulting average values for the strength and critical strain are summarized in Table 1, along with averages for tests at the higher quasistatic rate, as well as Series B tests at both rates.

Table 1. AVERAGE VALUES OF PEAK COMPRESSIVE STRESS AND CRITICAL STRAIN IN QUASISTATIC TESTS

NOMINAL STRAIN RATE	PEAK STRESS (MPa)	CRITICAL STRAIN	NUMBER OF SPECIMENS
			SERIES A
$7.5(10^{-5})$ s^{-1}	65.1	0.0029	6
$7.5(10^{-3})$ s^{-1}	73.6	0.0033	3
			SERIES B
$7.5(10^{-5})$ s^{-1}	54.8	0.0027	8
$7.5(10^{-3})$ s^{-1}	65.6	0.0031	5

2.3.3 Dynamic SHPB Tests

Only one of the Series A dynamic tests showed a peak stress being reached before the collar began to act. The mechanical results for that test were obtained by using the procedure discussed in relation to Figures 4 to 6 in Section 2.2.2. In Figure 8 the dynamic stress-strain curve for Specimen A-28-1 shows a peak stress of 17.67 KSI (122 MPa) at a critical strain of 0.53 percent. The strain rate at the peak stress 125 s^{-1}. Significant collar action began at a strain of about 0.55 percent; the portion of the curve beyond this point is meaningless, and most of it has been omitted from the figure.

In order to get more mechanical test results on Batch A specimens, two additional series of tests were performed, designated as Series C and Series S, but these were on specimens that had been in storage for about a year, so that their properties may not be strictly comparable. Series C used three of these aged Batch A specimens to obtain three complete stress-strain curves, without interruption by a collar, so that the entire strain-softening regime was included. Figure 9 shows the 3 curves obtained at 3 different striker-bar impact speeds. The curves have been offset along the strain axis in order to plot them together.

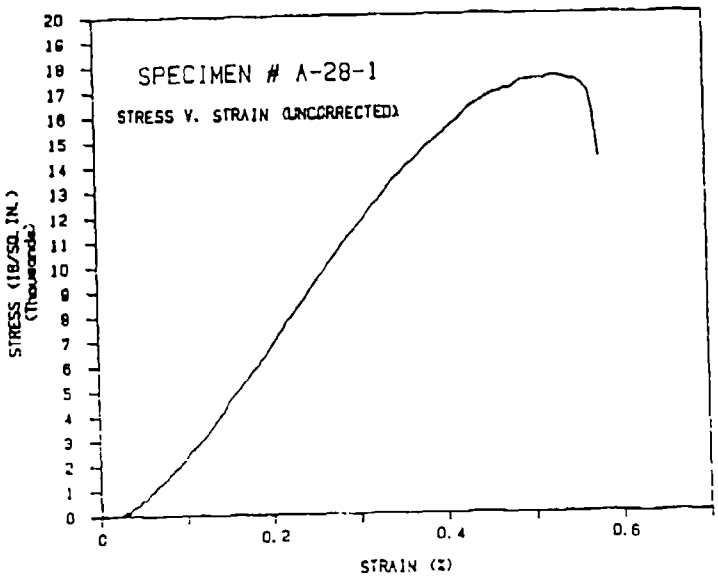

Figure 8. Dynamic Stress-Strain Curve for Specimen A-28-1.

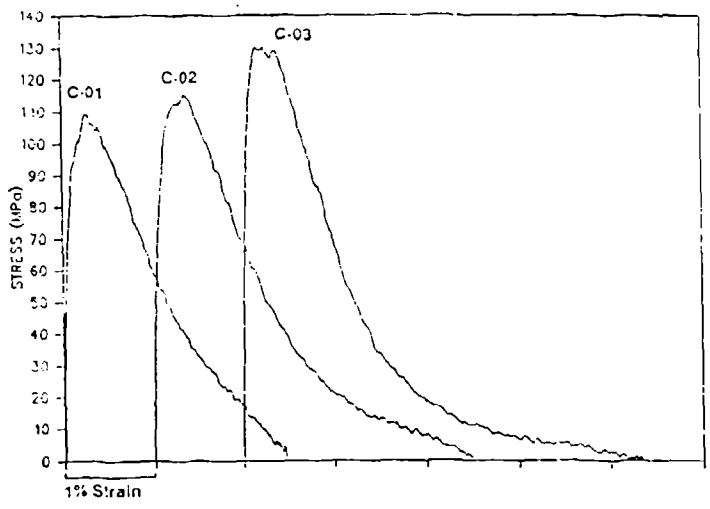

Figure 9. Complete Dynamic Stress-Strain Curves For Three one-year-old Batch A Specimens.

All the Series A and B dynamic tests were run at the same striker-bar impact speeds as Specimen C-02 in Figure 9. The one peak stress obtained in a Series A test agreed fairly well with the results for C-02, despite the additional aging for C-02, as will be shown in Table 2.

Series S used a shorter collar, in the hope that more data could be obtained on peak stress and critical strain at different strain rates before the collar interrupted the tests. Two different striker-bar impact speeds were used, corresponding to the highest and lowest speeds of the C series. The highest speed tests were designated S1, while the lowest speeds were designated S2. It turned out that, despite the shorter collar, only three S1 specimens and two S2 specimens furnished a clear peak stress before the collar action interrupted the tests. All the dynamic peak stress and critical strain data obtained from the tests are summarized in Table 2.

Table 2. PEAK STRESS AND CRITICAL STRAIN IN DYNAMIC TESTS

SPECIMEN NUMBER	PEAK STRESS (MPa)	CRITICAL STRAIN	STRAIN RATE AT PEAK (s^{-1})	GAS GUN PRESSURE (psi)
C-01	109	0.0045	54	190
S2-02	116	0.0052	66	190
S2-07	112	0.0059	57	190
C-02	115	0.0062	78	230
A-28-1	122	0.0053	125	230
C-03	130	0.0047	91	270
S1-01	121	0.0055	107	270
S1-02	108	0.0053	107	270
S1-03	118	0.0046	110	270

SECTION III
CRACK PATTERN OBSERVATION AND AUTOMATED IMAGE ANALYSIS

3.1 Introduction

Sample preparation is described in Section 3.2, and some examples of crack patterns are shown and discussed in Section 3.3. Automated image analysis procedures and results are presented in Sections 3.4 and 3.5, followed by discussion in Section 3.6.

3.2 Sample Preparation for Crack Pattern Observation and Analysis

Immediately after each specimen was tested, it was infiltrated with a high molecular weight methacrylate monomer solution with a fluorescent dye added, placed in a vacuum chamber for 15 minutes, and then kept at atmospheric pressure for one week to allow a full cure. See Appendix A for details of the specific infiltrant used and the procedure. The cured methacrylate stabilizes the sample mechanically; the fluorescent dye enhances contrast between cracks and matrix when viewed under ultraviolet light.

Specimens were then cut longitudinally with a diamond saw, and the rectangular central longitudinal sections thus exposed were polished on silicon carbide wet/dry grinding paper through 600 grit. Each section was final polished with 15 micron diamond paste on nap cloth on a polishing wheel until scratches were eliminated. After the polishing, each specimen was ultrasonically cleaned to remove all traces of loose fluorescent material.

Direct analysis of the crack patterns of the polished sections was not possible because of excessive camera response to the background areas. High-resolution macrographs of the polished sections were taken on black-and-white film through a 435-nm filter under ultraviolet light. The prints of these negatives exhibited strong contrast between the cracks filled with fluorescent dye and the matrix for these specimens where both the fine aggregate and the coarse aggregate were based on opaque Calera limestone as described in Section 2.2.1. High contrast is essential to the discrimination step in the automated image analysis.

3.3 Examples of Crack Patterns

The first series of tests on Batch A specimens included 20 dynamic SHPB tests with maximum axial strains varying from 0.001 to 0.008 and 21 quasistatic tests for comparison, performed in an MTS machine with maximum strains from 0.002 to 0.006. The range of maximum strains was obtained by grinding the specimens to a range of lengths slightly greater than the collar length, as described in Section 2.2.1. In the SHPB tests the incident bar inertia caused additional strain after the collar began to pick up the load.

Figure 10 shows examples of the crack patterns in central longitudinal sections, shown about 3/4 actual size for specimens of initial diameter 2 inches and initial heights from 1.622 to 1.628 inches. Two groups of selected specimens are shown to compare the general nature of the evolution of the cracks in static tests and dynamic tests. These are reduced photocopies of black-and-white photographs of the fluorescent-dye-enhanced sections, which were prepared as described in Section 3.2. The direction of loading is vertical in the figure.

The static series in the left-hand column of Figure 10 shows 5 specimens tested at a nominally constant compressive strain rate of 7.5×10^{-5} s^{-1} up to the time of collar contact. The maximum compressive strain reached in the test increased from about 0.002 for the top photo to 0.006 for the bottom one. The first two were stopped by the collar before any peak had been reached in the stress-strain curve. The third one was probably near a peak, while the last two were for maximum strains in the strain-softening regimes following peak stresses that occurred at critical strains of about 0.003. Evidently some cracks have appeared near the lateral surface before the critical strain is reached. As the maximum strain increases, the crack pattern becomes more prominent, spreading in toward the longitudinal axis and also showing greater crack density near the lateral surface. The cracks that develop during the static axial compression tests have some tendency to align with the testing direction, and individual cracks can sometimes be seen that run nearly the full length of the specimen.

In the static tests, even at a maximum strain of twice the critical strain, a small core near the axis shows no visible cracking.

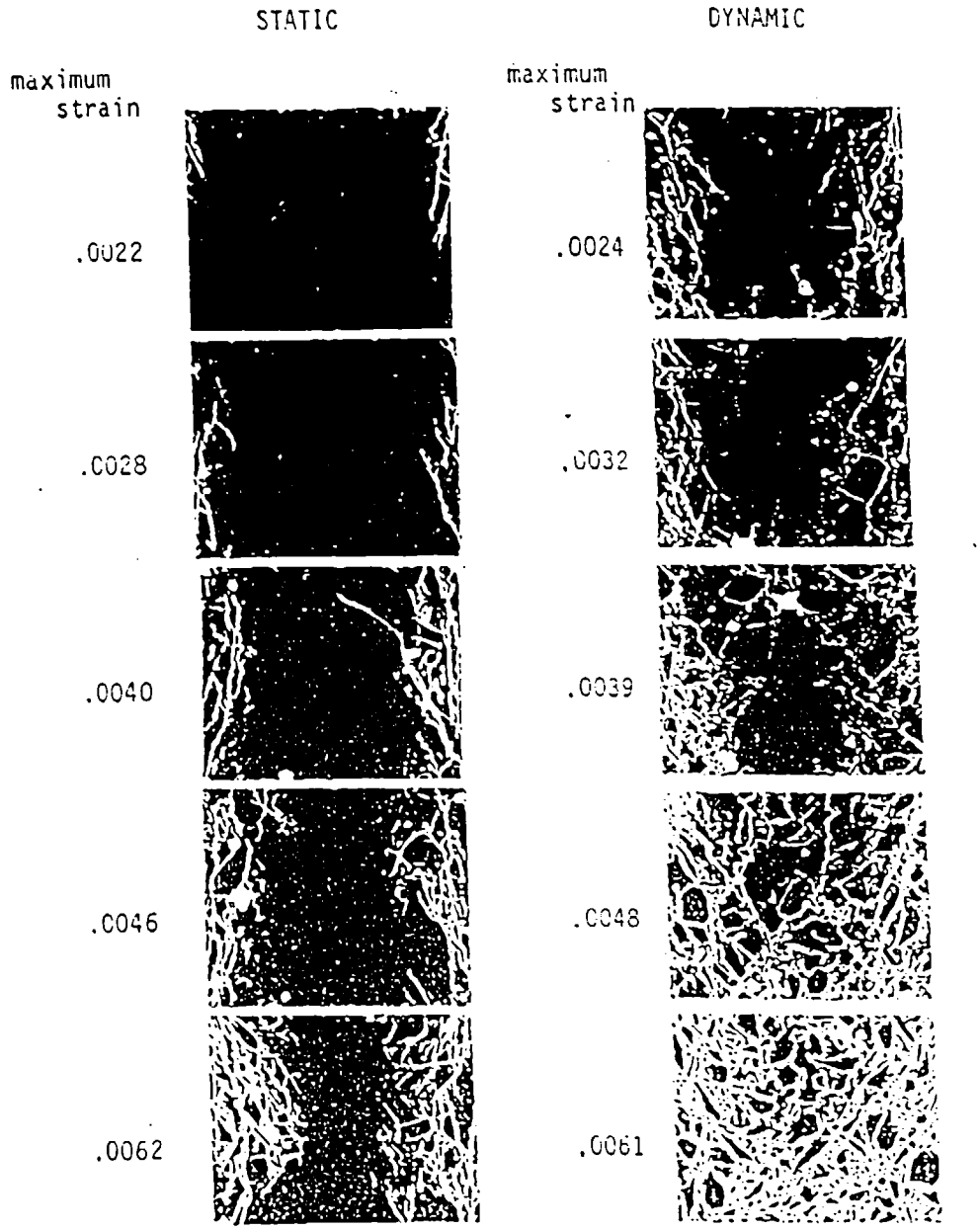

Figure 10. Longitudinal sections of selected static and dynamic test specimens, shown about 3/4 of full size. Testing direction is vertical and incident bar end is on bottom in dynamic tests.

The dynamic series in the right-hand column of Figure 10 is for 5 specimens tested in the SHPB, stopped by the collar at maximum strains comparable to those of the static tests in the left-hand column. The dynamic results show significantly more cracking than the static ones, up to 5 times as much crack length at low strains and more than twice as much at the higher strains, according to the automated image analysis. At the lower maximum strains cracks tend to concentrate in the outer zones of the specimen, near the lateral surface. By the third photo in the series the cracked area extends to the center at maximum strains greater than about 0.003, and in the last two the distribution appears fairly uniform throughout. Even at the earlier stages of the first two photos of the dynamic series, the distribution is denser and more uniform in the cracked portion of the section than in the static tests.

Because the collar interrupted all the dynamic tests shown in Figure 10 before any peak stress occurred, it is not possible to say what the critical strains were for these tests. The critical strain at the peak stress varied from 0.0045 to 0.0062 in the tests reported in Table 2 at the end of Section 2.3.2. This makes it plausible that the critical strain was never reached in the first three dynamic tests in the figure, and that it was reached while the collar was acting in the last two. The last two show more apparent crack-opening width than the first three. In the last one the entire mortar region looks like a sponge, with apparently almost every fine aggregate particle surrounded by open cracks. This specimen was recovered intact and, after infiltration with the monomer and curing, it had enough strength to endure the cutting and polishing before examination, but it seems unlikely that it would have had much load-carrying capacity without the infiltration and stabilization. In the discussion of the results of the image analysis in the following section it is suggested that, in the dynamic tests, a change in the nature of the crack density increase occurs to a behavior involving more connecting between existing cracks and less extension of existing cracks or creation of new

cracks when the crack density exceeds a certain amount. This transition occurred between the third and fourth photos of the dynamic series in Figure 10. It was suggested in Reference 17 that this change may represent some kind of failure of the specimen. According to that criterion, the last two dynamic examples in Figure 10 would have failed, which is consistent with the statement above that the last two may have reached or exceeded the critical strain.

These dynamic results seem to contradict observations by Ross, Reference 18, of high-speed photographic records of surface cracks in uninterrupted SHPB compression tests of concrete. In those tests, visible surface cracks first appeared at about the time when the peak stress was reached, while our results show cracking at the surface well before the critical strain was reached. It may be that the very fine cracks in the first photos of the dynamic series of Figure 10 show up in our results because of the fluorescent enhancement, but would not be visible in the high-speed photos of the surface, while the wider crack openings in the last two photos, which were for maximum strains greater than the critical strain, would show up in the high-speed photos of the surface cracks.

3.4 Automated Image Analysis Procedures for Characterization of Crack Structures

A Quantimet 520 image analysis system was used to capture, process, and analyze the photographs prepared as described in Section 3.2. Additional processing steps not available on the Q520 system were carried out by transporting the files containing the detected binary images to a VAX computer and developing programs for the purpose.

The photographic images were input to the Q520 system through an on-line video camera. The resulting digitized grey shade image is stored in a file. Cracks were detected and segmented from the matrix by setting a threshold level corresponding to a grey shade which is seen to fill in the crack domains on the displayed image.

The resulting binary (black-white) thresholded image was saved to a file and forms the basis for the analysis of the geometry of the cracks.

The crack images in the photographs have varying breadth. In order to obtain less ambiguous measures of the elements in the crack structure it was decided to perform the measurements on the *skeleton* of the crack network. The skeleton of a feature is obtained by systematically removing pixels from the outline of the feature (called an *erosion* of the feature) until the next erosion step would disconnect the feature. The result is a connected node-branch lineal network that represents the shape and topology of the feature. Although skeletonization routines are available on many image analysis systems our Q520 system does not possess this capability. Accordingly, a series of programs were developed to transfer the binary crack images generated in the Q520 to a VAX computer, skeletonize the image and analyze the result. These results were then transferred back to the Q520 system for display, further analysis and printing.

The results of this image processing are illustrated in Figures 11 through 15 [from Reference 17]. Figure 11 is the black-and-white photograph obtained under ultraviolet light. The detected binary image obtained from this input image is shown in Figure 12. The skeleton network generated from this binary image by the VAX computer program is displayed in Figure 13. Figure 14 is a superposition of the skeleton and binary images, illustrating how the skeleton network represents the crack structure. Figure 15 shows the skeleton network with branch points and end points identified and marked by implementing routines written for the VAX computer.

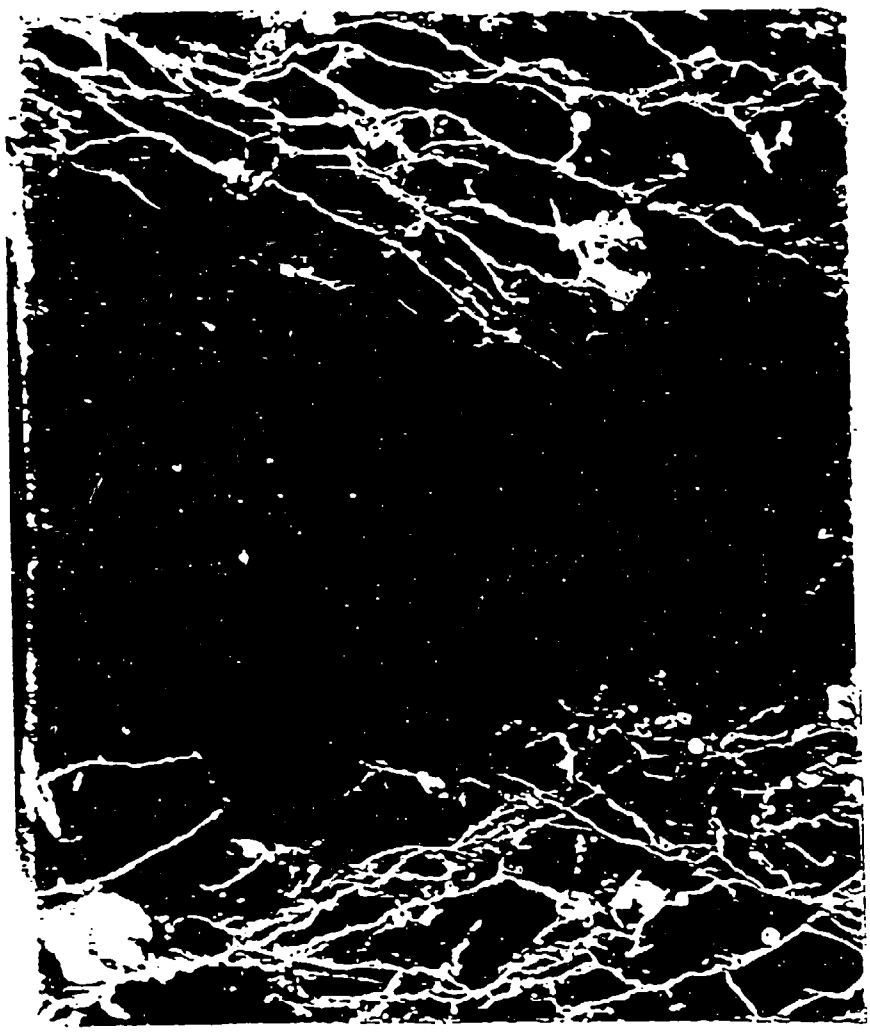

Figure 11. Macrograph of polished cross section of Specimen A-22-2, strained to 0.44 percent.

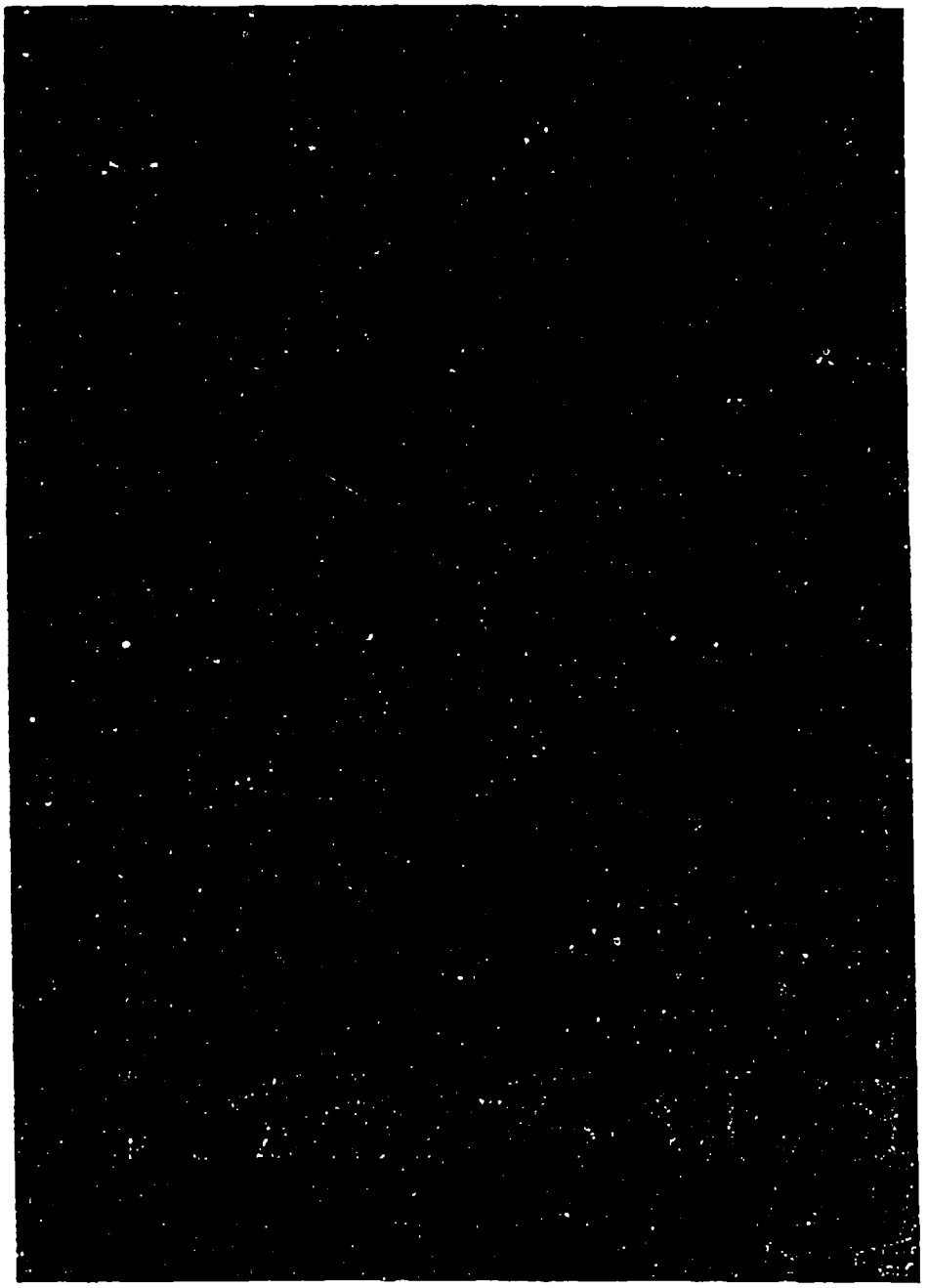

Figure 12. Digitized and detected binary image of one portion (about one quarter) of the crack structure shown in Figure 11.

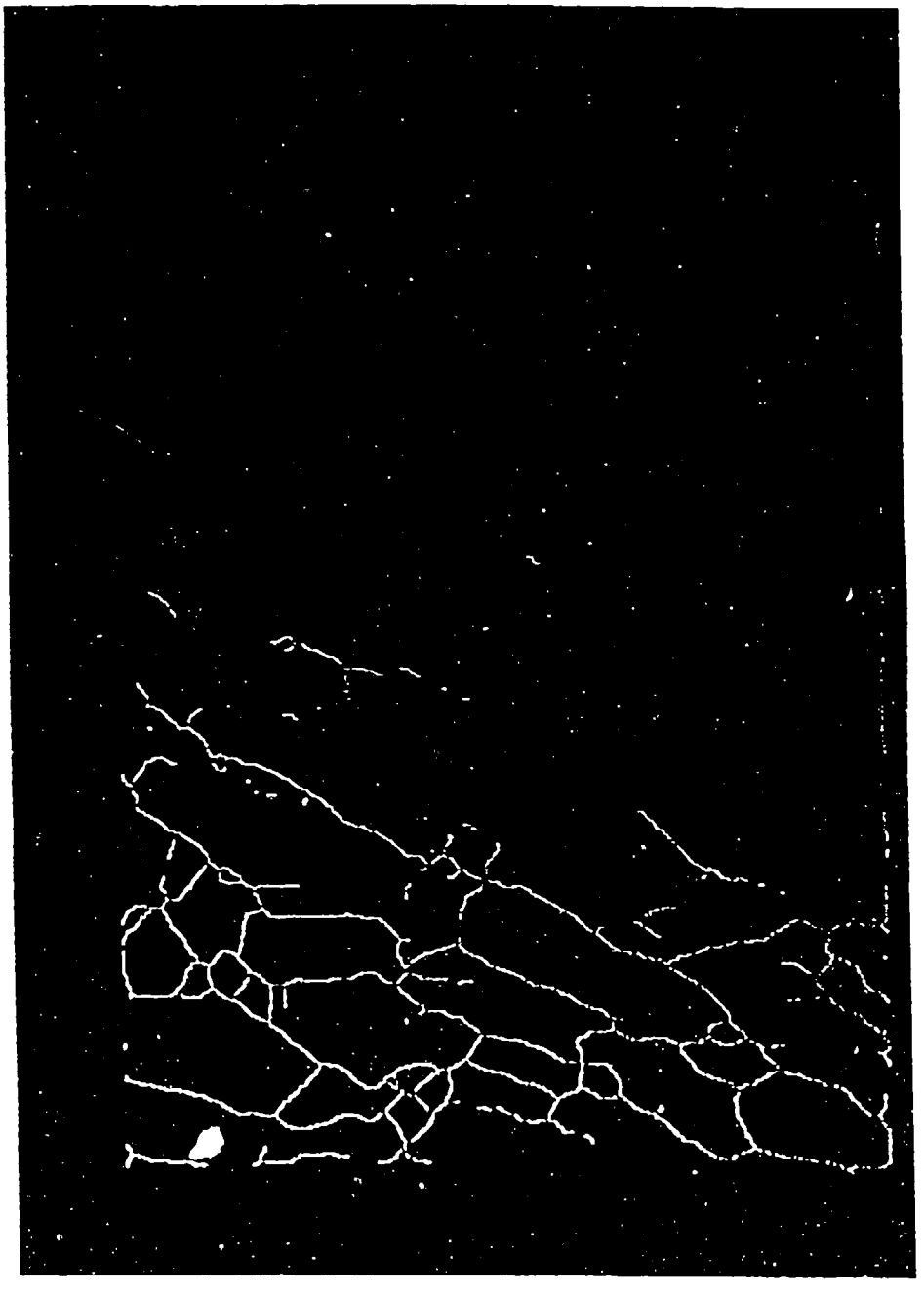

Figure 13. Skeleton of the binary image shown in Figure 12.

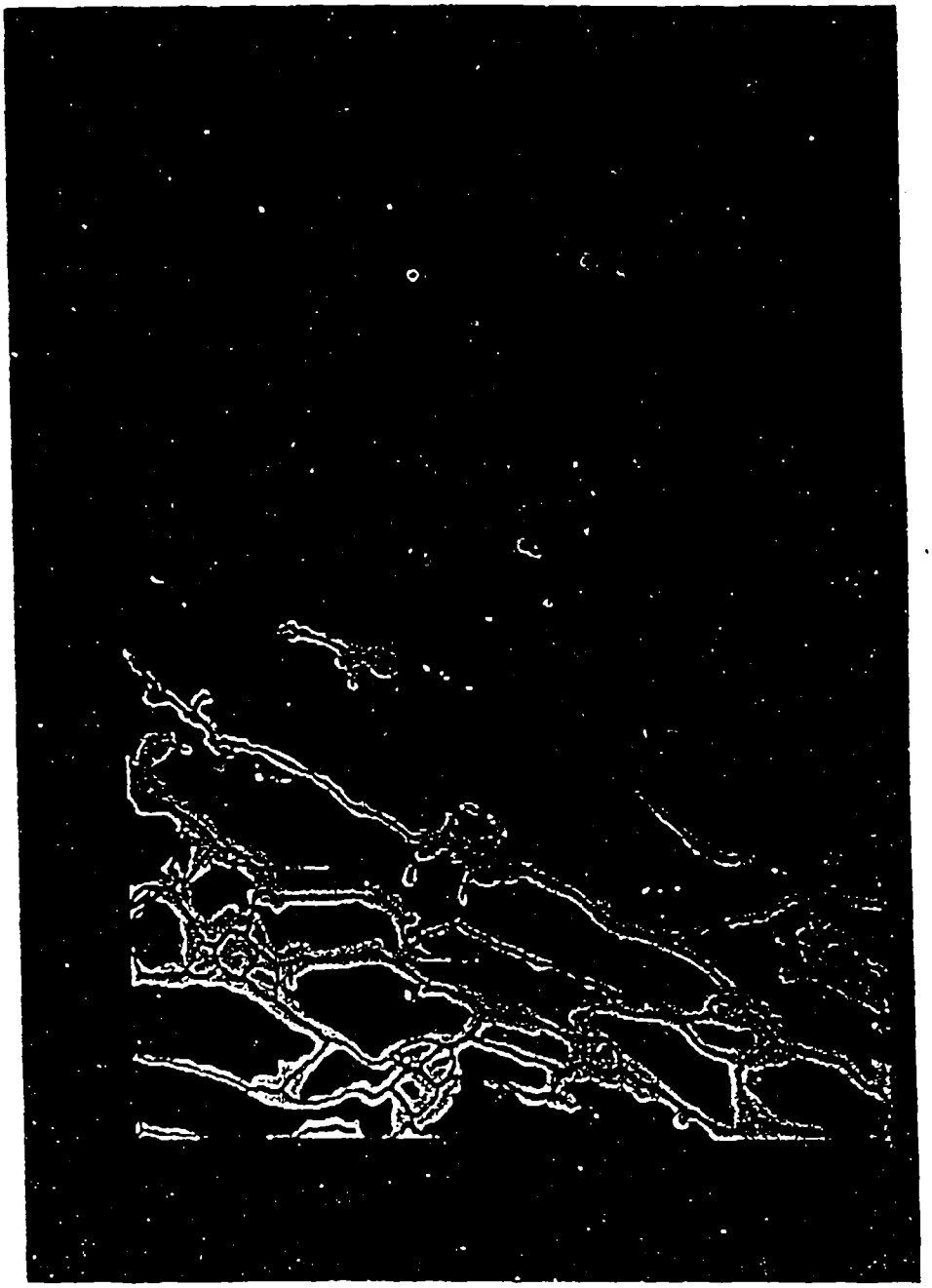

Figure 14. Comparison of the binary crack image and its skeleton.

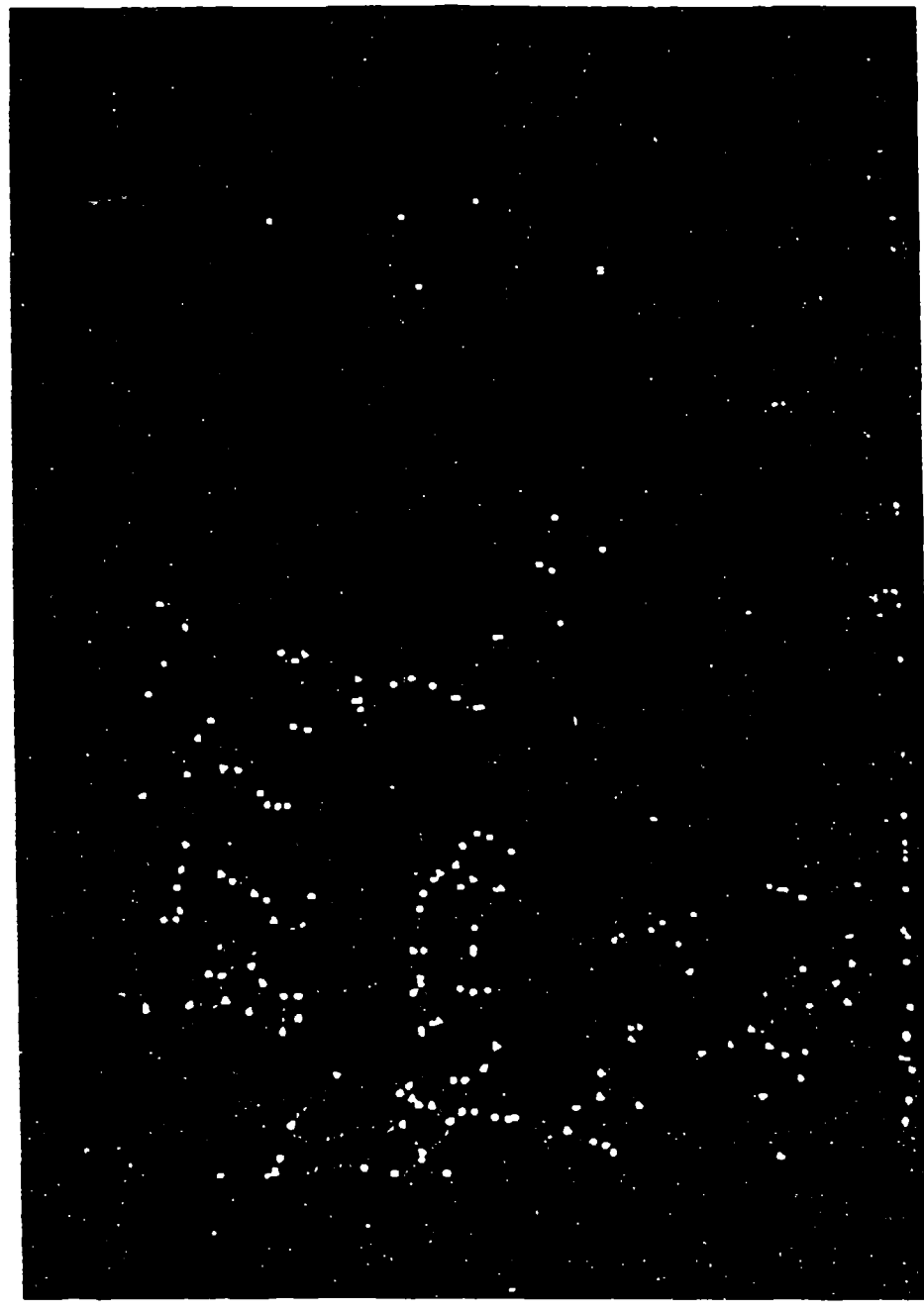

Figure 15. The skeleton of Figure 13 with the branch points and end points marked. In the Q520 display these are marked with different colors.

The quantitative characterization of the crack structure was implemented by making the following series of measurements on the skeletonized structure obtained from it:

a. $P_L(\theta)$, the number of intersections that a set of parallel test lines oriented at an angle θ to the vertical direction of axial loading makes with branches in the network structure, per unit length of test line. This quantity measures the total length of the projection of a lineal feature on a line perpendicular to the test lines, per unit area, References 19, and 20. Variation of P_L with θ, called the *rose-of-the-number-of-intersections*, provides a graphical illustration of the *anisotropy* of the lineal structure being sampled. An example is shown in Figure 16.

b. $\langle P_L \rangle$, the average of $P_L(\theta)$ over orientation is proportional to L_A, the total length per unit area of branches in the network according to the following stereological relationship [see References 19 and 20]:

$$\langle P_L \rangle = \frac{2}{\pi} L_A \qquad (1)$$

The total crack surface area per unit volume of structure is given by

$$\langle P_L \rangle = \frac{1}{2} S_V \qquad (2)$$

where $\langle P_L \rangle$ should be an appropriately weighted average of P_L, if P_L depends significantly on orientation.

c. $P_A{}^b$ is a count of the number of *branch points* in the network divided by the area scanned. A proper average of this quantity provides an estimate of the *length per unit volume* of crack branch lines in space:

$$P_A^b = \frac{1}{2} L_V^b \qquad (3)$$

d. P_A^e is a similar count of the number of crack *end points* per unit area sampled. This count is related to the length of crack edges in three dimensions, per unit volume,

$$P_A^e = \frac{1}{2} L_V^e \qquad (4)$$

e. The *degree of orientation*, ω, may be calculated in terms of the horizontal and vertical counts [References 19, 20]:

$$\omega = \frac{(P_L)_{max} - (P_L)_{min}}{(P_L)_{max} + (\frac{\pi}{2} - 1)(P_L)_{min}} \qquad (5)$$

3.5 Experimental Results of the Characterization Program

The quantities L_A, P_A^b, P_A^e, and ω were measured on the entire set of samples analyzed. The results for all the specimens from both Batch A and Batch B are tabulated in Appendix B [from Reference 17 with corrections made to the values of L_A given there]. The results from static tests are in Section 1 and the results from dynamic tests in Section 2 of Appendix B. Selected curves based on Batch A results will be presented in this section; for additional curves see Reference 17. Batch B samples with the higher water content show higher crack density than Batch A.

Anisotropy in the distribution of cracks in the longitudinal plane was characterized by measuring the rose-of-the-number-of-intersections. Figure 16, shows a typical rose, in this case for Specimen A-26-2 loaded statically to a strain of 0.55 percent. The longitudinal direction, which is vertical in this figure, gives a lower count than the horizontal direction. This implies that the projected length on a tangent plane (perpendicular to the radius of the cylindrical specimen) is larger than the projected length on a horizontal cross-section plane. Cracks evidently tend to align with the longitudinal axis, but the tendency is not pronounced. It is even less pronounced in the dynamically tested specimens, as will be seen in Figure 20.

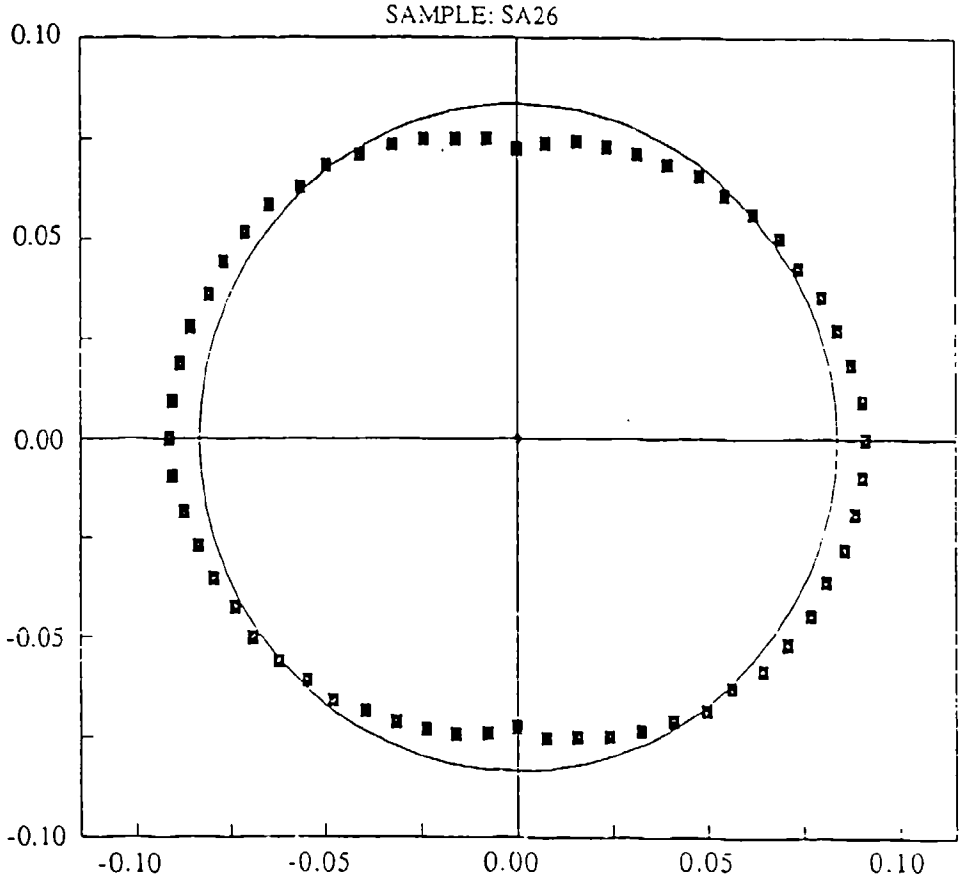

Figure 16. Typical rose-of-the-number-of intersections for Specimen A-26-2 strained statically to 0.55 percent strain

The stereological measurements furnish the evolution of the geometry of the crack structure with strain, as summarized in Figures 17 through 20 for all the static and dynamic tests of Batch A specimens, showing the evolution with strain of crack length per unit area L_A, branch point count per unit area P_A^1 . end point count

per unit area P_A^e, and degree of orientation ω, respectively. The first three measures increase roughly linearly with strain in each series (static or dynamic), but the counts are significantly higher throughout for the dynamic series than for the static series. The degree of orientation, ω, does not change significantly with the amount of strain, and is lower in the dynamic series than in the static series, averaging a value of about 0.2 in the static tests and about half that amount in the dynamic tests.

Useful insight into the damage development process is obtained by examining the *path* of evolution of the network. This treatment focuses upon how the geometric properties of the crack structure vary with each other. Total crack length, L_A, is taken as a measure of damage. The branch point counts and end point counts are plotted versus crack length in Figures 21 and 22.

3.6 Discussion of the Characterization Results

The general trends in the evolution of the crack structure presented in the preceding section are essentially as anticipated. Total crack length increases with strain whether testing is static or dynamic; the numbers of branch points and end points increase with the crack line length. The crack length data extrapolate to zero length at about 0.10% strain, indicating that a certain level of strain must be attained before cracks initiate, or at least become detectable at the scales of this examination. A similar correlation must exist for branch and end points.

A more interesting result appears in Figure 21, where the branch point density is plotted versus the crack density L_A for Batch A. Static and dynamic points fall essentially on the same curve, at least up the maximum L_A reached in the static tests. The dynamic branch point plot shows two changes of slope, the first near L_A = 0.62 mm/mm^2 [close to the maximum value reached in the static tests] and the second near L_A = 1.03 mm/mm^2, each indicating an increase in the branching rate. The dynamic end point count, Figure 22, also shows transitions at about the same two values of

L_A. Between the two transitions the end-point count shows almost no increase, while the branch point count increases faster; this implies that the increasing branch point count in this regime is a result of cracks connecting points on already existing cracks. Some extension of existing cracks may also be occurring without increaseing the end point count. Above the second transition near L_A = 1.03 mm/mm^2, the end point count increases again, implying some new cracks that do not connect points on existing cracks.

It has been conjectured, Reference 17, that the second transition represents failure. In the photo series of Figure 10 the first transition occurred between the second and third photo in the dynamic series, at a maximum strain of 0.003, and the second transition occurred between the third and fourth from the top at a maximum strain of 0.0047. From the photo series it appears that the first transition occurs when the central portion of the specimen, which was previously amost free of visible cracks, becomes involved. After the second transition both point counts increase, and there is a great deal of scatter in the end point data in this regime, which is presumably beyond the critical strain for failure.

These path correlations, plotting end and branch point counts versus crack length, show significantly less scatter than the correlations with strain. This suggests that the major component of variation that produces scatter in the data lies in the connection between strain and the crack length produced. Also, there is less scatter in the data for dynamically tested samples than for those in the static series.

The effect of strain rate was shown in Figures 17 through 20. Figure 17 showed that, at the same level of strain, dynamically loaded samples generate about twice the crack line length as do statically tested ones. Further, at this macroscopic level of detection, cracks initiate at a smaller strain in the dynamic tests. End and branch point counts show a similar rate dependence. Figure 20 shows a degree of orientation of about 0.2 for static tests and about 0.1 for dynamic tests, independent of the strain.

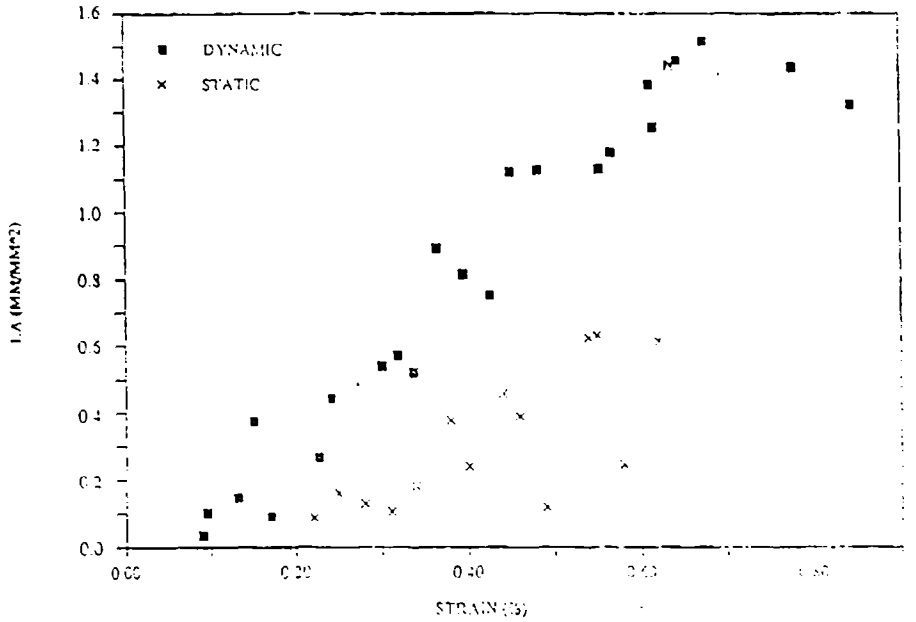

Figure 17. Comparison of crack length per unit area, L_A, versus strain for static and dynamic tests of Batch A.

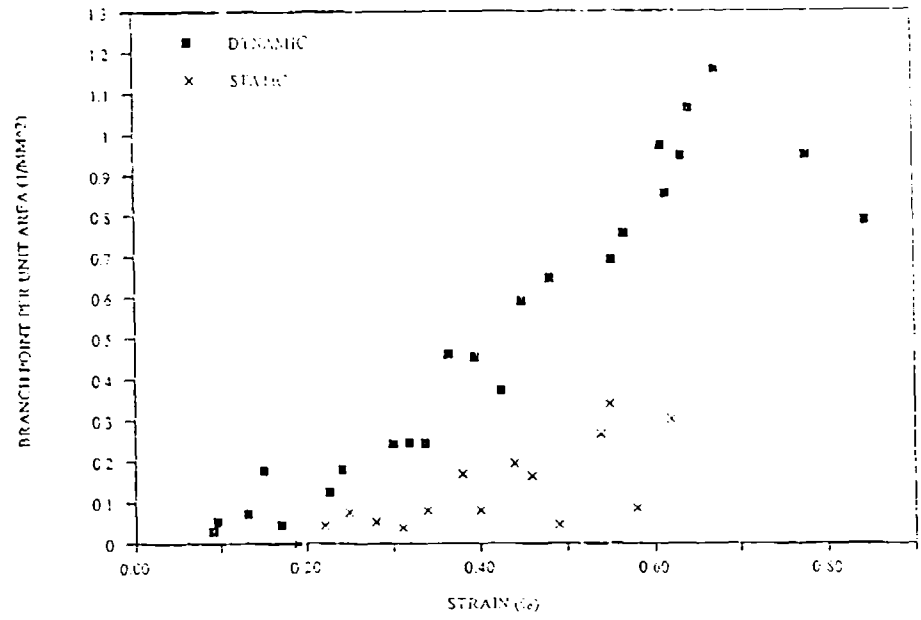

Figure 18. Comparison of P_A^b versus strain for static and dynamic tests of Batch A.

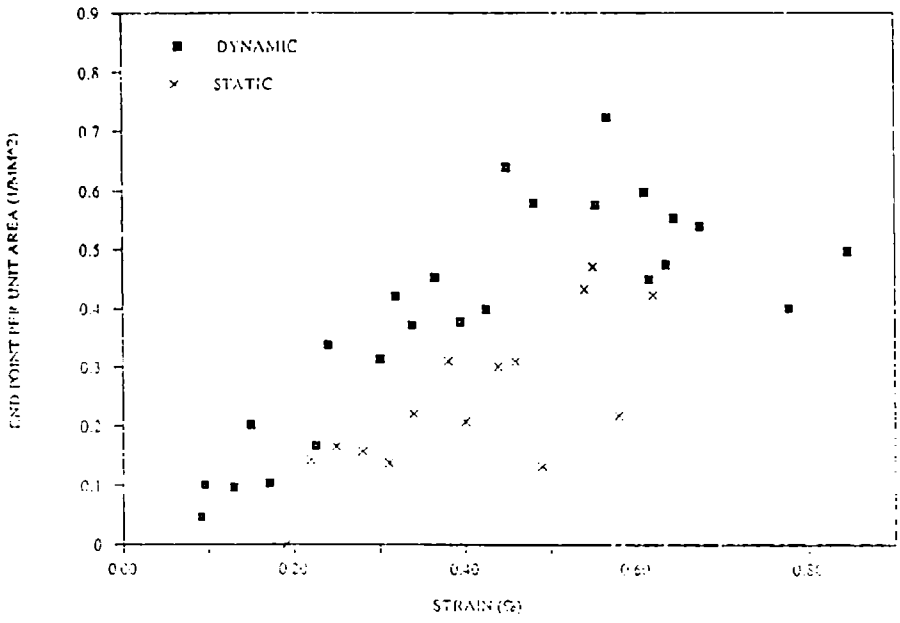

Figure 19. Comparison of P_A^e versus strain for static and dynamic tests of Batch A.

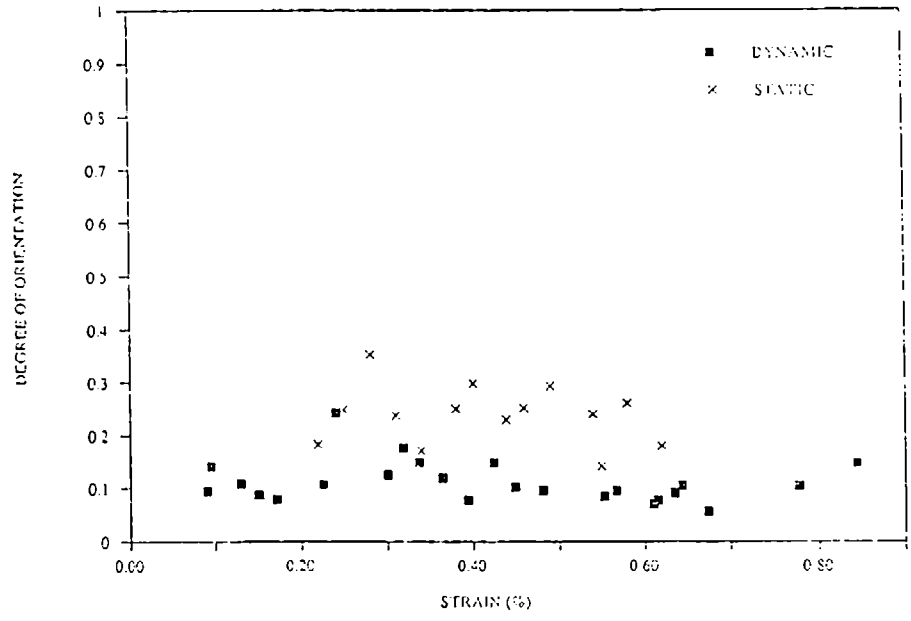

Figure 20. Comparison of degree of orientation, ω, versus strain for static and dynamic tests of Batch A.

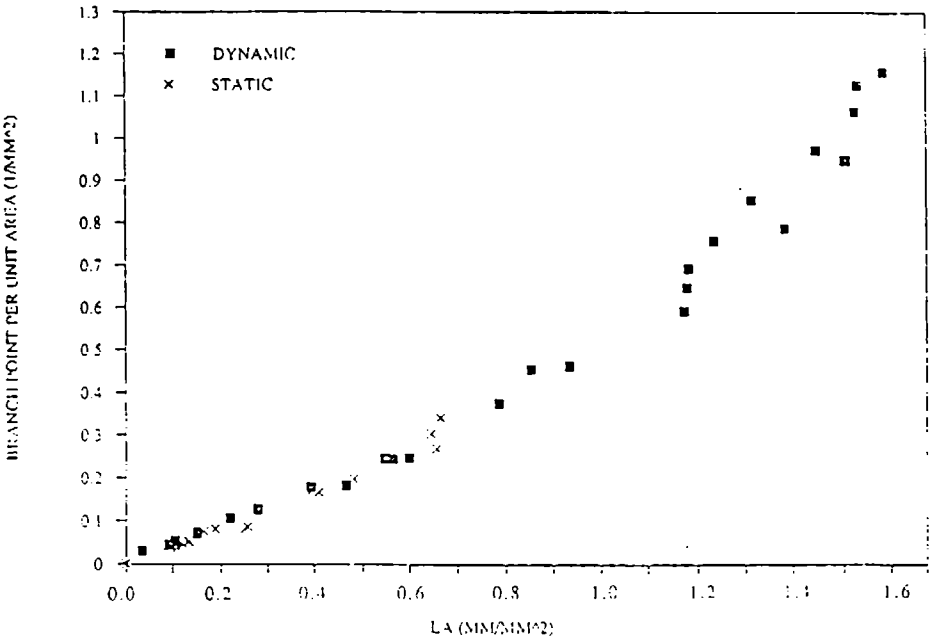

Figure 21. Variation of P_A^b with L_A for static and dynamic tests of Batch A.

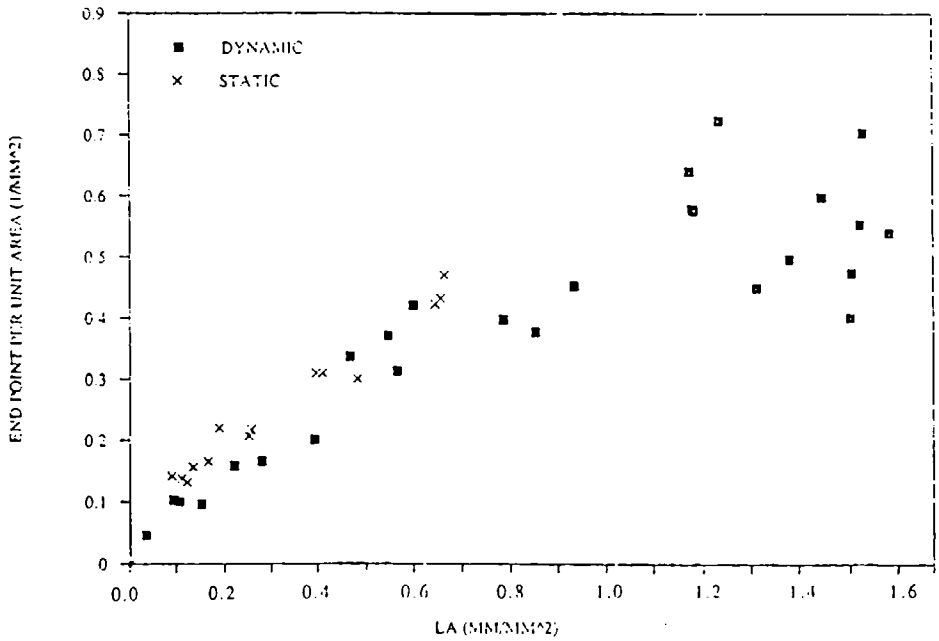

Figure 22. Variation of P_A^e with L_A for static and dynamic tests of Batch A.

The most straightforward and also strongest correlations are observed in the *path plots*, Figures 21 and 22. Both correlations are very tight. Direct comparison is limited to crack lengths that are less than about 0.62 mm/mm^2 because that is the value at the highest maximum strain reached in the static tests. Nonetheless, in the range where comparison is possible:

a. The data sets for static and dynamic testing *coincide;*
b. The correlations are linear; and
c. They extrapolate through zero.

The correlations for Batch B samples [not shown] tend to fall slightly below those for Batch A. These results make it evident that the *path* of evolution of the crack structures, i.e., the sequence of geometric states traversed, is slightly dependent upon the water content and resulting differences between batch A and batch B structures. More importantly, for a given batch the path is *independent of the strain rate*. The density of branch points and end points per unit length of crack line is established early in the process and is maintained. Below L_A = 0.62 mm/mm^2 the correlations are well described by:

$$P_A^e = 0.70\left(\frac{1}{mm}\right) L_A \qquad (6)$$

and

$$P_A^b = 0.41\left(\frac{1}{mm}\right) L_A \qquad (7)$$

The number of branch segments, B_A, per unit area in the network can be calculated by equation (8), if it is assumed that all branching nodes are triple points. Then the average length $\langle\lambda\rangle$ for Batch A samples is given by (9).

$$B_A = \frac{3}{2} P_A^b + \frac{1}{2} P_A^e \qquad (8)$$

$$\langle\lambda\rangle = \frac{L_A}{B_A} = \frac{L_A}{\frac{3}{2}(0.41)L_A + \frac{1}{2}(0.70)L_A} = 1.04\ mm \qquad (9)$$

For batch B samples this number is slightly larger: 1.29 mm. Since all correlations are linear, within each batch this number is independent of strain and strain rate, at least for values of L_A up to 0.62 mm/mm^2.

The picture of crack evolution that emerges from these correlations visualizes cracks initiating near the surface of the sample and propagating more or less isotropically inward. During propagation, at intervals that average about 1 mm for Batch A, the cracks branch. This spacing between branching events is independent of strain. Since the paths for static and dynamic tests coincide, this spacing is also independent of strain rate. However, it is slightly different for specimens drawn from the two batches, A and B. These observations are consistent with the conjecture that crack branching events are determined by the microstructure of the medium in which propagation is occurring, and not by the mechanics of the fracture process itself. It may be noted from the sieve analysis given in Appendix A that a considerable part of the aggregate consists of particles whose diameter is of the order of 1 mm.

These experimental results are reported as estimates of average values of the parameters, L_A, $P_A{}^b$ and $P_A{}^e$, for the longitudinal sections observed. They are geometric properties of that plane section through the sample. Comparison of these values for samples strained to different levels at different rates provides insight into the role played by these factors in the evolution of the crack structure.

A more fundamental understanding of this process could be obtained from information about the corresponding three dimensional geometric properties: S_V, the crack surface area per unit volume; $L_V{}^b$ the total length of branch lines per unit volume; and $L_V{}^e$ the total length of crack ends, per unit volume.

These three dimensional properties may be estimated from values for P_L, $P_A{}^b$ and $P_A{}^e$ by applying equations (2) to (4). These fundamental stereological relationships are, however, based upon the assumption that the test lines and test planes included in the sample analyzed form an "IUR" sample of the three dimensional structure; the test entities must form an **I**sotopic, **U**niform, **R**andom selection from the population of test lines in the case of P_L, and of test planes for P_A. If the structure being analyzed is itself isotropic and uniform, then any plane section or test line position and orientation will provide an unbiased sample.

The longitudinal sections examined in this study do not satisfy the requirements of a representative IUR sample because the crack structure clearly exhibits a variation with *position* in the sample. Because the process initiates near the outside surface and proceeds radially inward, the densities of all three measurements vary significantly with radius in each sample. All the data reported are simple averages over the area of the longitudinal section. However, measurements made in an interval r to r + Δr near the surface of the cylindrical sample represent a volume of material that is much larger than the same interval in r sampled near the central axis.

In order to provide unbiased estimates of the three-dimensional geometric prcperties, a more sophisticated sampling procedure must be designed and incorporated into the analysis. The longitudinal sectional area should be divided into a number of vertical strips and values for P_L, $P_A{}^b$ and $P_A{}^e$ measured in each strip, i.e., as a function of r_i, the radial coordinate of the strip. In obtaining an appropriate average value, these individual strip readings should be weighted by the square of the corresponding r_1 since the cylindrical volume each represents increases with the square of the distance from the longitudinal axis [References 19 and 20]. Thus, for example, an appropriate average value of P_A for insertion in equation (3) or (4) would be provided by the following equation (10).

$$\langle P_A \rangle = \frac{\sum_{i=1}^{n} (P_A)_i r_i^2}{\sum_{i=1}^{n} r_i^2} \qquad (10)$$

Figures 23(a) through 23(c) show an example of the results of a manual measurement of the variation of each of the three counting measurements with position along the radius of the sample. The counts were made for 13 equal radial intervals. The last one, on the right side of the figure, is for the interval adjacent to the outer boundary of the specimen of radius r. This particular sample was strained to 0.44 percent under static conditions. All three counts are largest near the surface of the cylinder and drop essentially to zero at the center. The line intercept and branch point counts (a) and (b) decline rapidly from the surface and drop to zero at about 0.4r. The endpoint count (c) scatters about a more or less constant value before dropping to zero at about 0.2r. Figures 23(d) and 23(e) plot the other two counts versus the line intercept count L_i. Interestingly, the radial variations of branch point and line intercept counts are strongly and linearly correlated, Figure 23(e). This lends further support to the notion that the spacing between branch lines on the evolving crack surface is fairly constant and probably determined by the microstructure of the medium.

A simple average value of the three counts has been used to make all the comparisons in this report. It was pointed out, however, that to provide an unbiased estimate of three dimensional measures, the weighted averaging procedure shown in equation (10) must be used for P_L, $P_A{}^b$ and $P_A{}^e$. Table 3 compares the unweighted and weighted averages for sample A-22-2 based on the data used in generating Figure 23. The bias due to the variation with radius shows clearly in this table with weighted averages consistently and significantly higher than the unweighted averages.

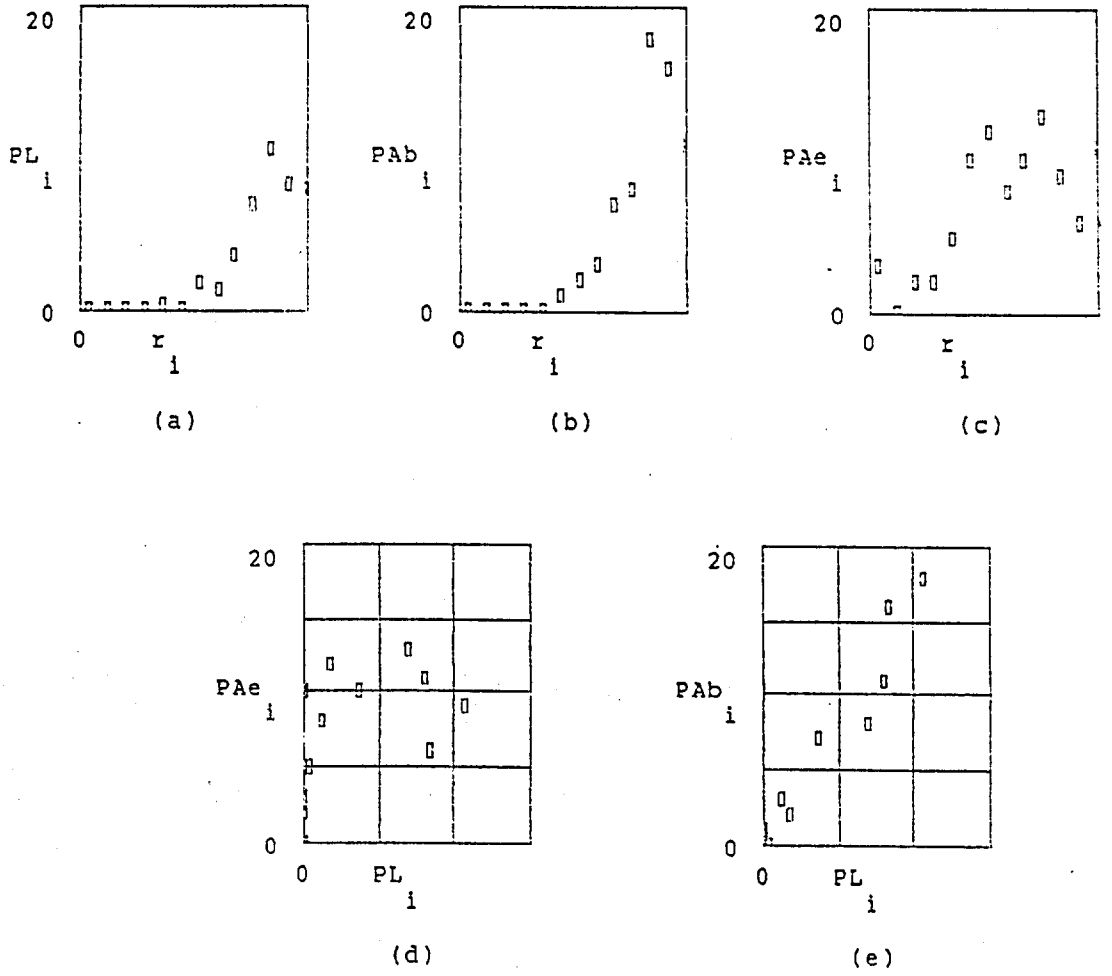

Figure 23 (a),(b),(c) Variation of the three counts with radius for Sample A-22-2. (d) and (e) Variation of the end and branch point counts, versus the corresponding line intercept count.

Also shown in Table 3 are unbiased estimates of crack surface area, S_V, branch line length, L_V^b and crack edge length, L_V^e, per unit volume, computed from equations (2) to (4) by using the weighted averages. These results make it clear that the use of unweighted averages of the stereological counting measurements does not provide unbiased estimates of the three dimensional geometric properties. Determination of the counting measurements as a function of radius on each sample would be required to obtain valid estimates of three dimensional geometric properties. This could be accomplished by automated image analysis procedures, but it has not yet been done.

When the crack pattern exhibits such a significant variation with position as do most of the static specimens in these tests, even a properly weighted average like that of equation (10) may not be adequate for application to the whole section, as was done in getting the numbers for Table 3. More meaningful would be averages over separate zones in the section, which might correspond to representative volume elements for a numerical analysis of the deformation process with a proposed constitutive model. This is clearly beyond the scope of the investigation reported here.

Table 3. WEIGHTED AND UNWEIGHTED AVERAGES FOR SAMPLE A-22-2

Point Count	Unweighted Average	Weighted Average	Unbiased Estimate
P_L (1/mm)	0.153	0.303	$S_V = 0.61$
P_A^b (1/mm^2)	0.127	0.25	$L_V^b = 0.50$
P_A^e (1/mm^2)	0.174	0.232	$L_V^e = 0.46$

The estimates per unit volume have the same units as the corresponding point counts.

SECTION IV

CONSTITUTIVE MODELS BASED ON CONTINUUM DAMAGE MECHANICS

4.1 Introduction

Most attempts to model the nonlinear stress-strain behavior of concrete and rock since about 1980 have been influenced by the 1976 paper by Budiansky and O'Connell, Reference 21, which calculated the effective elastic moduli of bodies containing randomly distributed flat cracks under various assumptions. The analysis is made for tensile loading with all the cracks open. The most often quoted results from this paper are for an isotropic distribution of circular cracks, for which simple formulas are given for the effective isotropic elastic moduli in terms of the moduli of the uncracked solid and a crack density parameter. Some of these results are summarized in Section 4.2. To build a constitutive model based on these results, it is necessary to know or to assume how the crack density parameter varies with inelastic deformation.

The continuum damage models to be discussed in Sections 4.3 and 4.4 are formulated in terms of internal state variables characterizing the state of the material, and evolution equations are introduced for the internal state variables. In the simplest of these models, it is assumed that only one scalar state variable is needed, which could be based on the crack density parameter. In applying this it is necessary to distinguish between open cracks and closed cracks under the prescribed loading. Most of the applications have been to tensile loading, but there have been applications to compression.

A phenomenological continuum damage model with a single internal state variable, which has been used with a rate-dependent evolution equation, is discussed in Section 4.3. The micromechanics-inspired models discussed in Section 4.4 do not furnish any rate dependent results that would account for the higher dynamic strengths reported in Section 2.3.2. The relevance of the crack pattern results that were presented in Section III to these models is considered in Section 4.5.

4.2 Effective Elastic Moduli of a Cracked Solid

Budiansky and O'Connell, Reference 21, used a self-consistent approach that sought to take an approximate account of the influence of crack interaction in calculating the effective elastic moduli of a body containing many flat cracks. The uncracked material was assumed to be locally isotropic, and the statistical distribution of the sizes, shapes, locations and orientations of the cracks were assumed to be sufficiently random and uncorrelated to make the cracked body isotropic and homogeneous in the large. Crack closure effects were ignored, so that sufficiently small stresses do not produce contact between the crack faces. The macroscopic incremental stress-strain relation for the cracked body is then linear, if the crack distribution does not change during the increment.

An overbar will denote an effective elastic property of the cracked solid; thus $\bar{K}/K$ is the ratio of the effective bulk modulus in a representative volume element to the bulk modulus of the uncracked material. For a random distribution of arbitrary flat cracks, their analysis gives

$$\frac{\bar{K}}{K} = 1 - [2N\langle a^3 f(\bar{\nu})\rangle]/[3(1-2\bar{\nu})] \qquad (11)$$

where

N is the number of cracks per unit volume

a is a characteristic linear dimension of the crack

$\bar{\nu}$ is the effective Poisson's ratio

f is a shape factor, depending upon the shape of the crack and also upon $\bar{\nu}$, and

$\langle\ \rangle$ denotes the average over the volume element.

If the statistical distributions of shape and size are uncorrelated, $N\langle a^3 f\rangle$ may be replaced by $N\langle a^3\rangle\langle f\rangle$. Note that the quantity $N\langle a^3\rangle$ is nondimensional, and, if all cracks have the same shape, this is the controlling statistical quantity. Indeed, we shall see that the proposed crack density parameter reduces to $N\langle a^3\rangle$ for circular cracks of radius a.

For elliptical cracks, all with the same aspect ratio, b/a, the shape function, f, is given by Budiansky and O'Connell as

$$f(\bar{\nu}) = \frac{4\pi}{3}\left(\frac{b}{a}\right)^2\left(\frac{1-\bar{\nu}^2}{E(k)}\right) \tag{11}$$

where E(k) is the complete elliptic integral of the second kind and $k = [1 - (b/a)^2]^{1/2}$. The crack area A and perimeter P are

$A = \pi ab$ and $P = 4aE(k)$.

The nondimensional crack density parameter ϵ was defined by

$$\epsilon = (2N/\pi)\langle A^2/P\rangle. \tag{13}$$

for elliptical cracks all having the same aspect ratio b/a. It was also shown that ϵ was an explicit function of $\bar{\nu}$, ν and a nondimensional quantity $T(b/a,\bar{\nu})$ given by a complicated expression involving elliptic integrals, such that its limit as the effective Poisson's ratio approaches zero is $T(b/a,0) = 2$.

The effective moduli all approach zero as ϵ approaches the value 9/16. This indicates a loss of coherence of the material, produced by the intersecting crack network, at the critical value $\epsilon = 9/16$. Budiansky and O'Connell said, "Although sufficient cracking will indeed have such an effect, it is clearly beyond the power of the self-consistent approach to predict the critical condition with precision." They remarked that it was plausible that very small stiffness will occur near $\epsilon = 9/16$.

For circular cracks, (b/a) = 1, the dependence on elliptical integrals disappears, and T and ϵ are given by explicit functions of the effective Poisson's ratio. The result for ϵ is

$$\epsilon = \frac{45}{16}\frac{(\nu-\bar{\nu})(2-\bar{\nu})}{(1-\bar{\nu}^2)[10\nu-\bar{\nu}(1+3\nu)]} \tag{14}$$

where ϵ is defined by

$$\epsilon = N\langle a^3\rangle. \tag{15}$$

The effective bulk modulus, Young's modulus and shear modulus are all given by simple formulas in the case of circular cracks; see equations (16), 17) and (18). The equation (16) for the effective bulk modulus is the same as was given for elliptical cracks.

$$\frac{\bar{K}}{K} = 1 - \frac{16}{9}[(1-\bar{\nu}^2)/(1-2\bar{\nu})]\,\epsilon \tag{16}$$

$$\frac{\bar{E}}{E} = 1 - \frac{16}{45}[(1-\bar{\nu}^2)(10-3\bar{\nu})/(2-\bar{\nu})]\epsilon \tag{17}$$

$$\frac{\bar{G}}{G} = 1 - \frac{32}{45}[(1-\bar{\nu})(5-\bar{\nu})/(2-\bar{\nu})]\epsilon \tag{18}$$

Simple formulas were also given in Reference 21 for long narrow elliptical cracks and for long narrow rectangular cracks (limiting cases as the aspect ratio approaches zero). It was considered likely that the results for circular cracks might even be applicable to all cracks of convex shape, with the understanding that the definition (13), in terms of area and perimeter of the crack, holds for ϵ.

4.3 A Phenomenological Continuum Damage Model Applicable to High-Rate Deformation

Taylor, Chen and Kuzmaul, Reference 22, proposed a continuum damage model for dynamic fracture of rock under tensile loading, in which the crack density parameter represents the volume fraction of material that has been stress-relieved by multiple crack growth. In their numerical implementation, they used J_2 flow theory of an elastic/perfectly plastic material for volumetric compressive loading and their damage model for regions of volumetric tension. While the theory was not capable of providing the crack opening displacements, it was assumed that the characteristic volume of a void is proportional to the characteristic length, a, cubed. Hence their crack density parameter C_D is given by

$$C_D = N(\beta a^3) \tag{19}$$

where ß is an unknown proportionality constant and N is the number of cracks per unit volume. Note the similarity to the crack density parameter ϵ given in equation (15) of Section 4.2 for a random distribution of circular cracks of radius a. Although Budiansky and O'Connell did not interpret ϵ as the void volume

fraction, it has those dimensions. Taylor et al. assumed that the material stiffness degradation was given in terms of their crack density parameter C_D by the same equations as those determined by Budiansky and O'Connell in terms of ϵ for circular cracks. Equations (16) and (14) of Section 4.2 become

$$\frac{\bar{K}}{K} = 1 - \frac{16}{9}[(1-\bar{\nu}^2)/(1-2\bar{\nu})]C_D \tag{20}$$

$$C_D = 1 - \frac{45}{16}\frac{(\nu-\bar{\nu})(2-\bar{\nu})}{(1-\bar{\nu}^2)[10\nu-\bar{\nu}(1+3\nu)]} \tag{21}$$

Taylor et al. followed Kipp and Grady, Reference 23, who used a Weibull distribution to determine the number of flaws that are active at a given mean tensile stress P, according to

$$N = k(P/3K)^m \tag{22}$$

where k and m are material constants to be determined experimentally. Based on energy considerations, Grady, Reference 24, derived an expression for the nominal fragment diameter, d, in dynamic fragmentation of a brittle material:

$$d = [\sqrt{20}K_{IC}/\rho C\dot{\epsilon}_{max}]^{2/3} \tag{23}$$

in terms of the mode I fracture toughness K_{IC}, the density ρ, the uniaxial stress wave speed (bar-wave speed) $C = (E/\rho)^{1/2}$ and the volumetric strain rate at fracture. They assumed that the characteristic initial flaw size, a, is proportional to the fragment radius d/2. Combining (19), (22) and (23) and absorbing the constant β into k then gives the following expression for the crack density parameter.

$$C_D = \frac{5}{2}\frac{k}{(3K)^m}\left(\frac{K_{IC}}{\rho C}\right)^2 P^m(\dot{\epsilon}_{max})^{-2} \tag{24}$$

If the material parameters k and m are known, then (24) gives C_D at fracture in terms of the mean stress P and the volumetric

strain rate at fracture. Then (21) can be solved as a cubic for the degraded Poisson's ratio, and (20) gives the degraded bulk modulus in terms of the degraded Poisson's ratio and C_D. They proposed to call the second term on the right side of (20) the damage, D:

Then (20) takes the simple form

$$\bar{K} = K(1-D) \tag{26}$$

The results given by Budiansky and O'Connell [equations (16) and (18) near the end of Section 4.2] indicate that a damage measure different from D would be needed for the degraded Young's modulus and the degraded shear modulus. Taylor et al. used the same D for both K and G, with the result that the spherical and deviatoric elastic stress-strain relations for the damaged material become

$$P = 3K(1 - D)\epsilon_v \tag{27}$$

$$S_{ij} = 2G(1 - D)e_{ij}. \tag{28}$$

In their numerical implementation of the model, they used a linear approximation to the inversion of equation (21), namely

$$\bar{\nu} = \nu(1 - \frac{16}{9}C_D) \tag{29}$$

which was shown to agree closely with the results of (21).

They suggested two different procedures for determining the material parameters k and m. The first procedure is used when laboratory data of fracture stress versus strain rate are available. They show that for constant volumetric strain rate, assuming $\nu = 0$,

$$\ln[P(t_m)] = C_o + \frac{2}{m}\ln(\dot{\epsilon}) \tag{30}$$

where $P(t_m)$ is the mean stress at the time t_m when the stress is

maximum, i.e. the fracture stress at constant mean strain rate. Two points on the experimental fracture-stress versus strain rate curve can then be used to determine the material parameter m.

Then k can be determined from another equation derived under the same simplifying assumptions:

$$\ln k = m\left(\ln\frac{3KM}{P(t_m)} - \frac{m+1}{m}\ln(m+1)\right) - \ln(A\dot{\epsilon}^{-2}) \qquad (31)$$

where A is given by

$$A = \frac{40}{9}\left(\frac{K_{IC}}{\rho C}\right)^2 \qquad (31)$$

If experimental data for fracture stress versus strain rate are not available, it is possible to generate these data by using an equation, which was derived by Kipp et al., Reference 25, for application to rock, and which has been adapted by Chen, Reference 26, for application to the dynamic tensile fracture of concrete, as follows.

$$\sigma_c = \left(\frac{9\pi E K_{IC}}{16 N_S{}^2 C_S}\right)^{1/3} \dot{\epsilon}^{1/3} \qquad (33)$$

Equation (33) relates the dynamic tensile strength σ_c to the strain rate. N_S is a shape factor (equal to 1.12 for circular cracks), C_s is the shear wave velocity, E is Young's modulus, and K_{IC} is the fracture toughness.

In their numerical application of the model to an oil-shale blasting experiment, Taylor et al., Reference 22, reported satisfactory agreement of the predicted arrival time and peak pressures with the record of a stress gauge grouted in place at a depth of 2.5 meters. The predicted region where the damage parameter had reached a value of 0.2 (which corresponded to the peak stress in a one-dimensional simulation) also agreed well with the region of loose material that was removed from the crater with

a backhoe. Chen, Reference 26, used the model to predict damage contours in concrete panels with an initial center crack, loaded in tension by a step load and by a ramp load, but did not have experimental data to compare with the predictions.

Chen, Reference 27, modified the model for application to biaxial quasistatic loading. The number, N, of activated cracks was assumed to be given by a Weibull distribution of the form

$$N = k'[(\epsilon_p)_{max}]^m \tag{34}$$

where $(\epsilon_p)_{max}$ is the maximum principal strain. Assuming again that C_D is proportional to the cube of the characteristic crack dimension, he derived a relationship of the form

$$C_D = k[(\epsilon_p)_{max}]^n \tag{35}$$

where k and n are now taken as the material parameters to be derived from experiments. A set of uniaxial and biaxial experimental stress-strain records was available in the literature. Chen used the uniaxial results to determine k and n; then he predicted two biaxial cases, which showed reasonable agreement in the rising portions of the axial stress versus axial strain curves. The model could predict beyond the peak stress into the strain-softening regime, but because the experiments were load controlled no experimental data were available for comparison in the strain softening regime. The modified model was also applied in Reference 28 to the uniaxial tensile loading of a center-cracked concrete panel.

All these versions of the phenomenological continuum damage model introduced in Reference 22 have been for tensile loading regions. Ross, Reference 18, has suggested that the dynamic model can be adapted to compressive data where the crack density is associated with a transverse tensile strain near the cylindrical bounding surfaces of an axial compression specimen. Some promising comparisons were made with experiments, but it was concluded that not enough good experimental data were available to determine the crack density parameter as a function of strain and strain rate.

Some of the continuum damage models in Section 4.4 have been adapted to compressive loading, for quasistatic conditions.

4.4 Continuum Damage Models Based on, or Inspired by, Micromechanics

4.4.1 Introduction

Continuum Damage Mechanics was reviewed by Krajcinovic in 1984 and 1986, References 29 and 30. Review papers have also been included in some more recent symposium publications; for example, References 31 and 32. Only a limited account will be presented here, based mainly on papers by Krajcinovic his colleagues, which appeared from 1981 through 1991. Continuum damage mechanics can be developed either as a memory type or as a state type of theory. Only the state type will be considered here, in which: (a) the response of the material depends only on the current microstructural arrangement, and (b) the microstructural arrangement can be described by a finite set of internal state variables.

For brittle materials, the damage is characterized by internal variables related to the arrangement of microcracks [and possibly also to macrocracks or mesocracks, if the crack development occurs in a compressive loading environment]. Most of the early work, and most of the models that have actually been applied, were based on a single scalar representation of the damage, as in the models discussed in Section 4.3. Others have proposed tensor internal variables, or additional components of the strain tensor, as internal variables; see citations in the review articles in References 29 to 32.

4.4.2 Phenomenological Model with a Vector Internal Variable

The representation of an array of flat planar microcracks by a vector internal variable was used by Krajcinovic and colleagues in References 33 and 34 in formulating a continuous damage theory of brittle materials, which was developed further and specifically addressed to concrete in Reference 35. They introduced a set of internal variables representing the damage in a smoothed sense, thus formulating a phenomenological theory inspired by micromechanics but ignoring the details of local stress distribution and the branching of cracks. The development of the theory was in

the framework of thermodynamics with internal variables [see literature citations in Reference 33].

For an isothermal process in a brittle material, the state functions were chosen in Reference 33 as the scalar Helmholtz free energy, ψ , and the stress tensor, σ. The only state variable for the isothermal reversible processes was the elastic strain tensor, ϵ, while the internal variables were the damage vectors. In Reference 35, the microcracks were assumed to be mostly flat and planar, and the damage was represented by a vector, $\omega = \omega \mathbf{n}$, such that, for small rotations

$$\dot{\omega}_i = (\dot{\omega} + \omega\dot{\theta})n_i \tag{36}$$

where ω is the relative void area in a cross section with normal $\mathbf{n}$, and θ is the angle which the normal to the damage field subtends with a fixed global (structural) coordinate system. This characterization of the damage in a real material with random microstructure implies several assumptions about proper averaging, choice of scale, etc.

The Helmholtz free energy for an isothermal process and small strains was assumed to be a function $\psi(\epsilon,\omega)$ of the elastic strain tensor and the damage vector. The stress is given by

$$\sigma_{IJ} = \rho\partial\psi/\partial\epsilon_{IJ} = K_{IJKL}\epsilon_{KL} \tag{37}$$

if ψ is assumed quadratic in the small strain components. The upper-case letter indices refer to the global structural coordinate system. Arguments based on the Clausius-Duhem inequality (second law of thermodynamics) then lead to the nonnegative dissipation power density per unit mass:

$$\dot{D} = \frac{1}{\rho} R_I \dot{\omega}_I \tag{38}$$

where the rate of change of ω_I is the kinematic variable (flux) and

$$R_I = -\rho\partial\psi/\partial\omega_I \tag{39}$$

is the thermodynamic force conjugate to the kinematic variable.

With some additional assumptions, this implies the existence of a scalar damage potential function, F, of the thermodynamic forces, such that the thermodynamic flux is given by

$$\dot{\omega}_m = \Lambda \, \partial F / \partial R_m \tag{40}$$

where Λ is an arbitrary factor selected so that (38) is satisfied. The advantage of this formulation of the constitutive equation for ω is that, instead of having to establish a series of functional relationships between the internal and state variables, one has only to determine a single scalar function, F(**R**). After the Helmholtz free energy has been chosen as a polynomial quadratic in strain and linear in the damage variable, the polynomial $\rho\psi$ is represented by making use of the irreducible integrity basis for representation of a polynomial scalar invariant function of a second order tensor and a vector. Details are omitted here; the representation contains three material parameters defining the influence of the microdefects on the state of the material.

The expressions for the thermodynamic forces, given by (39), take simple forms in the damage coordinate system (denoted by lower-case letter indices taking the values 1, 2, 3) in which the "1" axis is directed along the normal **n** to the damage plane, and "2" is along the resolved shear strain in the plane of the damage. Then $\omega_1 = \omega$ and $\omega_2 = \omega_3 = 0$. In the damage coordinates the scalar damage potential function is assumed to have the form

$$F = R_1^2 + a\omega R_2^2 - [R_o(\omega)]^2 \tag{41}$$

where a is a positive constant and $R_o(\omega)$ represents the recorded history.

In the Voigt notation (i.e., with components of stress and strain tensors arranged in column matrices), equation (37) takes the following form in the global coordinates

$$\sigma_I = K_{IJ} \epsilon_J \tag{42}$$

where the "elastic" matrix elements K_{IJ} are not constant, but

depend on the damage ω_M. Differentiation of (42) leads to the form given in (43). A further development, including transforming to the

$$\dot{\sigma}_I = K_{IJ}\dot{\epsilon}_J + D_{IM}\dot{\omega}_M \tag{43}$$

local damage coordinates and then back to the global system leads to equations of the forms given in (44) and (45).

$$\dot{\omega}_J = cM_{JK}\dot{\epsilon}_K \tag{44}$$

$$\dot{\omega}_I = (K_{IJ} + cD_{IL}M_{LJ})\dot{\epsilon}_J \tag{45}$$

where c is a switching coefficient, such that c = 1 for loading (in terms of damage growth), i.e.

$$c = 1 \quad iff \quad F = 0 \quad and \quad \frac{\partial F}{\partial R_m}\dot{R}_m > 0 \tag{46}$$

otherwise c = 0

The applicability of the theory was tested on cases of unconfined uniaxial compression and tension of concrete specimens. The damage potential function F of equation (41) was simplified by assuming that R_o was linear in ω: $R_o = \omega/G_o$ where G_o is a constant. Three other material constants, K_i, also appeared in the representations of the damaged stiffness matrix K_{IJ} in terms of the damage ω, a lengthy development, which is omitted here. For compression of initially isotropic material in the x-direction, it was assumed that $\omega_x = 0$, while $\omega_y = \omega_z = \omega$.

The four constants, K_1, K_2, K_3, and G_o, were chosen to fit experimental compression data for 3 grades of concrete. The K_i were chosen the same for all 3 grades, since they define the state and should not change substantially from one grade to another.

The same values of the constants were used to predict uniaxial tension response, where the microcracks were assumed to be perpendicular to the loading x-direction, so that

$$\omega_x = \omega \qquad \text{and} \qquad \omega_y = \omega_z = 0.$$

The predicted stress-strain curves in uniaxial tension were said to

follow experimentally established trends, although no tensile experimental data were presented for the 3 grades of concrete.

4.4.3 Micromechanics-Based Damage Models

Between 1986 and 1991 Krajcinovic and his colleagues published a number of papers proposing a micromechanics based damage model for brittle materials, which would be a closer representation of real behavior than the phenomenological model described above; see, for example, References 37-41. Only a brief descriptive account of the methodology will be given here with almost all the mathematical details omitted.

Reference 37 was specifically addressed to concrete. It began by recognizing three structural scales: On the microscale in the cement paste, the defects are atomic voids and crystal defects. The mesoscale consists of a unit cell containing a statistically valid sample of phases; the defects are microcracks and large pores, and it is described by micromechanical models. The macroscale is the entire concrete specimen; the defect is a macrocrack, and it is modeled by continuum theories and fracture mechanics. It was suggested that a suitable unit cell for the mesoscale in concrete might contain 30-100 aggregates. Their macro classification was probably motivated by experience with tensile loading, where failure usually occurs by one big crack. Our experimental observations with small compression specimens suggest that there may be some overlap between mesocracks and macrocracks.

In developing the governing equations, the small strain tensor was represented by the sum of two integrals representing volume averages, one over the volume V_m occupied by the matrix within the unit cell, and one over the volume V_i of the cracks within the units cell, calculated by making use of a representation of the displacement discontinuity vector,

$\mathbf{b} = [\mathbf{u}]$ across the crack with normal $\mathbf{n}$.

Microcracks are present in concrete even before the first load is applied. After an initial microcrack is subjected to tensile or shear stress it will at a certain load level become unstable. According to the Griffiths model, once a crack is activated in a

homogeneous stress field in a homogeneous material it will spread catastrophically. Experience indicates, however, that activation of defects on the mesoscale in concrete does not signal the imminence of catastrophic failure. Initial defects in concrete are typically located on facets of the interface between an aggregate and the cement paste. In uniaxial tension, the first ones activated are likely to be on facets whose normal is not too far from the tensile load direction. When one is activated, it spreads until it reaches the edge of the facet, where it is stopped by the cement paste's higher critical stress intensity factor. Observations indicate, in fact, that most stable microcracks in concrete are of a size comparable to that of an aggregate facet.

For vertical tensile loading, let q denote the external stress, q_o its value when the first crack is activated, for example, on a horizontal facet of maximum size, and q_1 the external stress when some of the arrested cracks start propagating again through the cement paste. [Simple formulas are given in Reference 37 in terms of critical stress intensity factors and dimensions.] When the crack starts propagating in an unstable manner through the cement paste, final failure is probably imminent, although the crack could be temporarily arrested by an impediment.

The seemingly gradual accumulation of damage is possible only as a result of a rather random distribution of defects, weak planes, and crack arresting barriers. Because of the randomness, the cracks are destabilized sequentially as the external load increases. This gradual process appears smooth on the macroscopic scale, but, as acoustic emission tests have indicated, microcracking on the mesoscale is actually a spasmodic process. Some randomness of the geometry on the mesoscale is an essential aspect of the problem. Analytical artifices such as assuming perfect honeycomb arrangement of regular hexagonal grains are inherently incapable of modeling the process.

An illustrative example was given in Reference 37 for a prismatic concrete specimen loaded in tension. The components of the 4th-order compliance tensor $\mathbf{S}$ were determined as the sum of the

compliances representing elastic compliance of the matrix, and two representing the displacement discontinuities associated with the unstable cracks and the stable cracks. In the absence of the exact sieving curve for the tested concrete specimens, they assumed a band-limited, uniform probability function for the linear dimension of the crack. Details of the development are omitted here.

The results were plotted as a normalized tensile stress-strain curve. For external axial stress q, the ordinate was q/q_o and the abscissa was the axial strain divided by its value when $q = q_o$. The results was a straight line up to (1,1), and in fact neither the calculated nor the experimental curve deviated far from the straight line in the limited range to which the curve was shown (up to about $q/q_o = 1.2$, where the normalized strain was 1.25. The experimental curve showed a slightly higher stress at the end than did the analytical curve, but they were very close. Curves were also given for the predicted apparent Poisson's ratio and for the effects on the stress-strain curve of variations in the sieve grading and of variations in the size of initial bleeding defects.

In their conclusion the authors say, "The major objective of the proposed model is to demonstrate that it is possible to formulate a rational constitutive model without introducing a large number of unidentifiable 'material constants.' Most importantly, the proposed model proves that a kinetic law can be actually derived on the basis of a proper description of the mesostructure and the relative toughness of the constituent phases." "Naturally, the model relates the macrostructural response of the solid with the mesostructure (volume fraction of coarse aggregate, sieving curve, etc.)." At this stage the model was limited to monotonically increasing proportional load (no crack changes its status from active to passive). This development in Reference 37 was focused on tensile loading.

The main objective in Reference 38 was to formulate a general three-dimensional micromechanical model for concrete subjected to multiaxial compressive loads. Above a certain value of the axial compressive force, the faces of pre-existing interfacial defects

undergo Mode II cracking, which is ultimately arrested at the edge of the aggregate facet by the tougher cement paste. In the model it is assumed that the pre-existing microcracks which are located on the aggregate paste interfaces have the isotropic distribution

$$2a_o = \rho^2 D \tag{47}$$

where $2a_o$ is the diameter of the penny-shaped crack, D is the effective diameter of the aggregate facet, and ρ is a scalar less than one that defines the fraction of the facet that is initially debonded.

Consider an example where the facet is inclined at some angle θ to the vertical axis of compression loading. For uniaxial or triaxial compression below the brittle-ductile transition, it has been observed that the diameter of the Mode II microcrack increases from $2a_o$ to D when a certain axial stress is obtained; the axial stress required increases with the amount of lateral stress confinement. The transition from $2a_o$ to D is unstable, but the crack is arrested at the edge of the interface by the tougher cement paste. As the axial stress increases further, the frictional sliding cracks initiate tension cracks at their tips. These tension cracks kink from the original sliding direction and eventually align themselves with the axial direction. The propagation of these kinked cracks is unstable if the lateral stress is tensile, but stable if the lateral stress is compressive.

Since in the absence of lateral tension a single kinked crack grows in a stable manner, the ultimate failure must occur as a result of a preferentially oriented band of kinked cracks. This instability onset problem was not addressed.

Each interface crack is subjected to both a normal and a shear stress. By taking account of friction, the authors develop an expression for the stresses on a typical crack in terms of the axial compressive stress q, the lateral compressive stress q*, the coefficient of friction μ, and the angle θ that the crack normal makes with the vertical. Once the faces of a crack are able to slide relative to each other, the size of the crack will increase when the Mode II stress intensity factor becomes equal to the

critical Mode II stress intensity factor for the interface. This leads to a value of q at which the crack is activated. Consideration of a distribution of sizes and orientations leads to the definition of q_c as the value of q for which the first pre-existing crack is activated. The value of the required q_o increases with the magnitude of the lateral compressive stress q*.

Since the actual problem is not amenable to closed form solution, it was assumed that the 3-dimensional problem can be approximated by a series of 2-dimensional sections. Details of this procedure and the rest of the development are omitted. As in Reference 37, the small strain is calculated by two averaging procedures, one of the elastic strain averaged over the matrix volume and one related to the active cracks. This leads to a representation

$$\epsilon_{ik} = S_{ikmn}\sigma_{km} \tag{48}$$

where the 4th-order compliance tensor $\mathbf{S}$ contains both the elastic compliance of the matrix, $\mathbf{S}^e$, and the effects of the pre-existing cracks.

The model developed was tested by its ability to reproduce some experimental results in two cases, one of uniaxial compression and one of triaxial compression with a small lateral confining pressure, q* = 500 psi. For each case, the axial, volumetric and lateral strains were plotted versus the axial stress, and the apparent Poisson's ratio was plotted versus the axial strain. Agreement between the analytical and experimental curves was good.

In principle the model is applicable to all plain concrete mixes of normal weight. It would be necessary to modify the model in the case of large aggregate volume fractions, since the pre-existing cracks would be located closer to each other and thus interact.

A different approach to micromechanically based damage models for brittle materials was taken by Krajcinovic and colleagues in References 39-41, making use of fracture mechanics concepts such as strain energy release rate, G, and surface energy, γ. The development was again in the framework of continuum thermodynamics

with internal variables, as in the phenomenological model of Section 4.4.2, but using the dual Gibbs potential density function, instead of the Helmholtz free energy. If the Gibbs function is denoted by $\psi(\sigma,T,H)$, where σ is the stress tensor, T is temperature and H denotes parameters defining the history of the deformation, then the strain is given by

$$\epsilon = \partial\psi/\partial\sigma \qquad \text{(H constant)} \tag{49}$$

which under certain assumptions leads to an equation like (48).

If $\delta l(L)$ denotes the advance of a crack front, L, in the direction of its normal, the energy, dD, dissipated on the creation of new surfaces can be written as

$$dD = \int_L 2\gamma\ \delta l\ dL \tag{50}$$

where γ is the surface energy. Since the energy release rate G is defined as

$$G = -(\partial\psi/\partial l) \tag{51}$$

the second law of thermodynamics for this process takes the form

$$\int_L (G - 2\gamma)\,\delta l\ dL \geq 0 \tag{52}$$

which is often assumed to be satisfied pointwise on L, leading to the more common form of the instability criterion

$$(G-2\gamma)\,\delta l > 0 \tag{53}$$

Further details of the development will not be given here. In Reference 41 some examples of discrete statistical models were discussed, and it was suggested that their generalization to real microstructures might provide good bases for micromechanical models for brittle deformation processes. The statistical (discrete) modeling was limited to expensive computation, which will become even more extensive with transition to three-dimensional problems and more realistic lattices.

The authors of Reference 41 concluded that the micromechanical modeling seems to work well for homogeneous states of stress and

strain and the pre-critical regime, and finally said that "The most far reaching conclusion is, perhaps, that the deterministic nature of the pre-critical response lends itself well to micromechanical and phenomenological modeling alike."

4.4.4 A Micromechanics-Inspired Phenomenological Model

A phenomenological model more closely based on the micromechanical considerations of References 37 to 41 was proposed in Reference 42. In a development like that of equations (48) to (52), the irreversible change $d^i\psi$ of the Gibbs energy is

$$d^i\psi = \langle (G - 2\gamma)\, dA \rangle \tag{54}$$

where the angular brackets denote the average along the crack length L, while dA = L dl is the increment of crack surface area. This suggested the choice of thermodynamic force (or affinity), f_α, and corresponding flux, ξ_α, for each mode, as

$$f_\alpha = \frac{L}{2A}\langle G - 2\gamma \rangle_\alpha \qquad d\xi_\alpha = \frac{1}{V}\left\langle \frac{2A\, dA}{L} \right\rangle_\alpha \tag{55}$$

In (55), f_α is the excess strain energy release rate integrated along the perimeter and averaged over the crack surface area, while $d\xi_\alpha$ is recognized as the increment of the Budiansky-O'Connell damage variable. For self-similar growth of penny-shaped cracks, he flux can be integrated into the damage variable used in References 37 and 40.

For isothermal deformation of a brittle solid weakened by a large number of existing microcracks, the macro-response variables, $\mathbf{Q}$ and $d\mathbf{q}$, for the phenomenological theory were then chosen, within the framework of the self-consistent theory and for a homogeneous state of macrostress, so that

$$d^i\psi = \mathbf{Q} \bullet d\mathbf{q} = (1/2)\boldsymbol{\sigma} : d\mathbf{S} : \boldsymbol{\sigma} \tag{55}$$

Thus, referred to principal axes of stress, the affinities $\mathbf{Q}$ and fluxes $d\mathbf{q}$ are given as in equations (57) and (58).

$$2\mathbf{Q} = [\sigma_{11}^2,\ \sigma_{22}^2,\ \ldots] \tag{57}$$

$$d\mathbf{q} = [dS_{1111},\ dS_{2222},\ \ldots] \tag{58}$$

The change of compliance is measurable locally, making it a

useful choice for an internal variable. Because of the unilateral constraints placed on the displacement field by the cracks, it is only possible to identify the positive change of the compliance as the flux. Thus the compliance $\mathbf{S}$ is not strictly an internal variable, even though its positive increment is the flux. Then, when the increment $d\mathbf{S}^*$ is positive, the inelastic strain increment $d\boldsymbol{\epsilon}^*$ is given by

$$d\boldsymbol{\epsilon}^* = d\mathbf{S}^* : d\boldsymbol{\sigma}. \tag{59}$$

In a transition from an equilibrium state $(\boldsymbol{\sigma}, H)$ to a neighboring equilibrium state $(\boldsymbol{\sigma} + \delta\boldsymbol{\sigma}, H + \delta H)$, the change in Gibbs energy is

$$\delta\psi = \mathbf{S} : \delta\mathbf{Q} + (1/V) f_n \delta\xi_n \tag{60}$$

where $\mathbf{S} : \delta\mathbf{Q} = \boldsymbol{\epsilon} : \delta\boldsymbol{\sigma}$ is the work increment of surface forces on a unit cell, while the second term in (60) is the work increment of internal variables. If the increase of surface area of a particular crack depends only on the external stress through its own conjugate force,

$$\dot{\xi}_n = F(f_n, H), \tag{61}$$

it follows that the macropotential $\Omega(\mathbf{Q}, \xi)$ can be obtained [as in Rice, Reference 43] by superimposing all micropotentials $F(f_n, H)$. The macrofluxes are then given by (62).

$$\dot{S} = \frac{\partial\Omega(Q, \xi)}{\partial Q} \tag{62}$$

The proposed approximation ceases to be valid when the crack growth is dependent directly on the external stresses or when the direct interaction between the cracks becomes a dominant effect, such as during the final phase of the splitting of rocks or concrete [see Horii and Nemat-Nasser, Reference 44, and Kachanov, Reference 45].

The geometrical representation of the flow potential [damage surface] in the space of the affinities $\mathbf{Q}$ is analogous to the yield surface in plasticity. It may be viewed as a "singular clustering of surfaces of constant flow potential" [Rice, Reference 43].

In other words, the macropotential is an envelope of a polyhedral surface consisting of N planes, each representing conditions under which a particular crack commences growth. The development of the normality property, etc., follows the well-known results for the yield surface [see Rice, References 43 and 46]. The derivation of fluxes using the normality property is analogous to the determination of plastic strain rates. Deviations from normality are associated with frictional sliding losses [Rudnicki and Rice, Reference 47.]. The analysis ceases to be valid in the strain-softening regime.

Examples of the formulation were discussed in terms of an initial single crack embedded in an infinite homogeneous and isotropic elastic plate, subjected to a stress field with principal stresses σ_1 and σ_2. For the case of tensile stresses and an initial crack of length $2a_o$ inclined at angle θ to the direction of the larger tensile principal stress, σ_1, the inequality (53) leads to (63).

$$\frac{\pi}{E_o}(\sigma_1^2 cos^2\theta + \sigma_2^2 sin^2\theta) - 2\gamma \geq 0 \qquad (63)$$

With the affinities chosen as $Q_i = (1/2)\sigma_i^2$, with equality in (63) the equation represents a family of straight lines in Q_1, Q_2 space with θ as a parameter [representing many cracks, which act independently]. For an arbitrary stress pat. the first crack to become critical is perpendicular to the larger principal stress. The magnitude of the other principal stress has no influence on the onset of nonlinear behavior, but plays a role as the external tractions are further increased. Th shear stress assists in causing any extended crack to kink from its initial direction toward a direction perpendicular to the larger of the two tensile principal stresses. It was assumed that, at least at the beginning, only $dS_{1111} > 0$, while all other components of the compliance remain unaltered. The damage surface was assumed to consist of two perpendicular lines Q_1 = const. and Q_2 = const. intersecting at the initial isotropic point $Q_1 = Q_2$ at which crack

extension begins. This damage surface is the inner envelope of the family of lines defined by equality in (63). An illustrative example was presented for uniaxial tension in concrete, with good agreement between theory and experiment for the axial stress versus strain.

The compression case is more difficult. The kinked crack in a compressive field can be treated much in the same manner as the tensile crack. The results of micromechanical analyses by Horii and Nemat-Nasser, Reference 44 and Nemat-Nasser and Obata, Reference 48, for a single crack in an infinite plate at angle θ to the larger compressive principal stress, were used as a guidance for formulating a simple representation of the damage surface in terms of macro variables. Details are omitted here. A numerical example for uniaxial compression σ_1, with $\sigma_2 = 0$, and all slits assumed perpendicular to the third axis, so that a two-dimensional analysis was possible, was compared with some experimental results for a triaxial test with $\sigma_2 = 0$ and $\sigma_3 = \sigma_1/3$. Good agreement between theory and experiment was shown in plots of both ϵ_1 and ϵ_2 versus σ_1.

Krajcinovic et al., Reference 42, concluded that "The proposed framework for the development of a phenomenological model is consistent with the micromechanics of brittle deformation processes in addition to satisfying the requirements of thermodynamics." At this stage of development, problems considered were primarily dominated by tensile cracks; it was assumed that the energy dissipated by frictional sliding is negligible compared to the energy required for creation of new internal surfaces in the material. As a consequence, it was possible to use the normality property of the damage potential and greatly simplify the analyses. "In the future the proposed model must be tested on three-dimensional cases, considering the interaction of brittle and ductile mechanisms. Current analyses are restricted to the pre-critical regime. Substantially more attention should be focused on the post-peak behavior in order to enable analyses of a general case of stress and geometry. In that sense this study is but a

basis for a more comprehensive effort which will hopefully follow in the future."

4.5 Relevance of our Experimental Results to Models

In the discussion of the experimental crack structure in Section 3.6, the crack density, L_A, [crack length per unit area of longitudinal section] appeared to be a significant damage measure. When other features of the damage were plotted versus L_A, the static and dynamic results essentially coincide, while the plots of L_A and the other features versus strain showed significant rate dependence. Toward the end of Section 3.6 it was pointed out how unbiased estimates of the volumetric density S_V, [crack surface per unit volume] could be obtained from the data for L_A. A crack density C_D proportional to the crack volume per unit volume could be determined by an averaging process similar to that for S_V by incorporating measurements of crack opening width, obtained by image analysis procedures. Although this has not been done, the implied relationship and our observation that L_A seems to be a good measure of the damage in our experiments furnish additional evidence that the parameter C_D used in the phenomenological models of Section 4.3 is an appropriate measure.

The parameter C_D was essentially the Budiansky-O'Connell parameter of Section 4.2 for penny-shaped cracks, which reappeared in the micromechanics-inspired phenomenological model of Section 4.4.4; see the discussion following equation (55). The flux in (55) was for microcracks on the mesoscale; see the discussion of scales in the second paragraph of Section 4.4.3. The macroscale was the entire concrete specimen, and the mesoscale consisted of a unit cell containing a statistically valid sample of phases.

The experimental crack pattern analyses in Section III [see figures 10 to 15] dealt with larger scale cracks than the initial microcracks whose extension was considered in the models of Section 4.4. Figure 11, for example, is only enlarged about 2.68 times the actual longitudinal section of the whole specimen. These should evidently be called macrocracks. Our results show a considerable

amount of macrocrack interaction and branching well before the peak stress is reached in both the static and dynamic unconfined compression tests. This implies stable crack growth, or possibly short unstable bursts interrupted by obstacles or by propagation into a region of compressive volumetric strain.

For the kinked microcrack propagation in axial compression, the micromechanical models presume unstable crack propagation when the lateral stress is tensile, and stable propagation when the lateral stress is compressive. This applies to the mesoscale. In our tests the macro lateral stress was zero, but the cracks were stopped even in the static tests, if the test was stopped before the peak stress was reached.

It does not seem likely that the models of Section 4.4 could be adapted to describe the rate dependence in high-rate tests. The thermodynamic treatment presumes that the deformation can be treated as a succession of equilibrium states. This could accommodate rate dependence in creep, but not the rapid loading of our dynamic tests.

Our experimental results indicate that the dependence of the other crack pattern features on the crack density, L_A, is determined by microstructural features such as aggregate particle sizes and distribution, and is essentially independent of the rate of deformation. This suggests that a phenomenological model based on a crack density similar to C_D could be applied to a compression-dominated deformation. The principal rate-dependence of such a model, which is yet to be proposed, would be in the evolution equation for C_D. At fixed C_D, the response would be essentially elastic, with damage-affected moduli. The evolution equation for C_D would have to be determined empirically, in the absence of a more fundamental theoretical basis. A form for the rate-dependent evolution equation could be assumed with a limited number of constants to be determined by suitable experiments. This is the same sort of procedure as was used in the models of Section 4.3 for tension-dominated high-rate deformation and for quasistatic compression.

SECTION V

CONCLUSIONS AND RECOMMENDATIONS

The following conclusions are supported by the results of the experimental investigations reported in Sections II and III, in which both static and dynamic tests on one particular concrete were interrupted by a steel collar that stopped the deformation, so that intact specimens could be examined for crack patterns. The particular concrete was prepared with both coarse and fine aggregate of opaque Calera limestone, so that automated image analysis of sections of damaged specimens infiltrated by a monomer containing a fluorescent dye was not confused by reflections from underneath the surface of the section being examined under ultraviolet light. The automated image analysis of the skeletonized crack patterns on central longitudinal sections of the damaged specimens provided average values of total crack length per unit area, L_A, number of branch points per unit area, $P_A{}^b$, and number of end points per unit area, $P_A{}^e$. The degree of orientation of the cracks was also determined.

CONCLUSIONS

1. Each of the three averages (of L_A, $P_A{}^b$ and $P_A{}^e$) increased roughly linearly with the maximum strain reached in static tests and in dynamic tests, but the values in the dynamic tests were significantly higher than the static values. The dynamic crack density L_A was more than twice the static value at each maximum strain level. There was no jump in the plots of L_A versus maximum strain where the critical strain (at peak stress) was exceeded.

2. The degree of orientation was independent of the maximum strain level reached in the interrupted tests. The dynamic crack patterns showed only a slight degree of orientation (about 0.1); the static values were about twice the dynamic value. A degree of orientation of 0 would imply isotropy; a value of 1 would imply all cracks aligned with the direction of axial compressive loading.

3. The cracks were not uniformly distributed over the longitudinal sections. At low levels of maximum strain, the crack patterns tend to cluster near the lateral surface of the specimen. For static tests, even at maximum strains twice the critical strain at peak stress the central region still showed no damage. For dynamic tests the pattern spreads inward more rapidly, and the whole section is involved at about the time the critical strain is reached. [These dynamic results seem to contradict observations by Ross, Reference 18, of high-speed photographic records of surface cracks in uninterrupted dynamic compression tests, where visible cracks first showed up at about the time of the peak stress. It may be that the very fine cracks before the peak stress showed up in our examinations because of the fluorescent enhancement, but would not show up in the high speed photos.]

4. The most significant result appeared when the branch point and end point counts were plotted versus the crack density, L_A. Comparisons between static and dynamic results are limited to values of L_A less than 0.62 mm/mm^2 because that is the value at the highest strain reached in the static tests. In the range where comparison was possible:

(a) **The static and dynamic plots coincide**,

(b) the plots are linear, and

(c) they extrapolate through zero.

The dynamic plots extend to higher values of L_A and show changes of slope at two points at values higher than those reached in the static tests.

5. The coincidence of the static and dynamic plots noted above strongly suggests that:

(a) The branching characteristics of the crack pattern are governed by the microstructure of the medium.

(b) All the rate dependence of the mechanical response is related to rate dependence in the evolution of a damage parameter related to the crack density L_A. [In the mechanical results the dynamic peak stresses (ultimate strengths) were up to 1.8 times the static values.]

6. Conclusions 4 and 5 suggest that a phenomenological constitutive model of the damage process might well be based on a crack density parameter C_D [crack volume per unit volume] related to L_A; see Section 4.5.

7. The literature review of some proposed constitutive models in Section IV did not find any that treated high-rate deformation in compression, although one phenomenological model for tension might possibly be adapted to compression. The more advanced micromechanics-inspired models seem to be limited by their basis in thermodynamics, which considers the deformation as a succession of equilibrium states.

RECOMMENDATIONS

1. Further experimental studies of this type should seek an improved procedure for interrupting the dynamic tests.

2. Additional sections should be examined in future tests to provide better data on inhomogeneity and orientation of the crack patterns in the three-dimensional specimen.

3. Additional automated image analyses of the longitudinal sections already prepared should be made to quantify the distribution over the sections, as suggested near the end of Section III and to determine crack-opening widths, as suggested in Section 4.5.

4. The possibility of a coordinated series of tests for determining parameters needed for a phenomenological model usable for high-rate deformation in a compression environment, with crack density as the basic damage parameter as suggested in Section 4.5, should be explored.

SECTION VI

REFERENCES

1. L. E. Malvern and D. A. Jenkins, Strength and Deformation of Confined and Unconfined Concrete Under Axial Dynamic Loading, Final Technical Report, Contract AFOSR-87-0201, University of Florida, 24 August 1988.

2. L. E. Malvern, D. A. Jenkins, T. Tang and J. C. Gong, "Dynamic Testing of Concrete with the Split Hopkinson Pressure Bar," Proc. Fourth International Symposium on the interaction of Non-nuclear Munitions with Structures, Panama City Beach, Florida, 17- 21 April 1989, pp. 296-301.

3. L. E. Malvern, T. Tang, D. A. Jenkins and J. C. Gong, "Dynamic Compressive Strength of Cementitious Materials," Materials Research Society, Symposium Proceedings, Vol. 64, eds. S. Mindess and S. P. Shah, Materials Research Society, Pittsburgh, PA. 1986. pp. 119-138.

4. L. E. Malvern and C. A. Ross, Dynamic Response of Concrete and Concrete Structures, Final Technical Report, Contact AFOSR F49620-83-K007, University of Florida, 30 May 1986.

5. L. E. Malvern, D. A. Jenkins, T. Tang and C. A. Ross, "Dynamic Compressive Testing of Concrete", Proc. Second Symposium on the Interaction of Non-Nuclear Munitions with Structures, Panama City Beach, Florida, April 15-19, 1985, pp. 194- 199.

6. J. C. Gong, L. E. Malvern and D. A. Jenkins, "Dispersion Investigation in the Split Hopkinson Pressure Bar," Journal of Engineering Materials and Technology, Transactions of the ASME, Vol 112, 1990, pp. 309-314.

7. T. Tang, Behavior of Concrete under Dynamic Compressive Loading, Ph. D. Dissertation, University of Florida, 1990.

8. J. C. Gong, Confined and Unconfined Compressive Strength and Deformation of Concrete at High Strain Rate, Ph. D. Dissertation, University of Florida, 1988.

9. L. E. Malvern and D. A. Jenkins, Dynamic Testing of Laterally Confined Concrete, Final Technical Report, AFESC Contract F08635-88-C-0194, University of Florida, 16 October 1989.

10. J. C. Gong and L. E. Malvern, "Passively Confined Tests of Axial Dynamic Compressive Strength of Concrete,"

Experimental Mechanics, Vol 30, 1990, pp. 55-60.

11. L. E. Malvern, D. A. Jenkins, T. Tang and S. McClure, "Dynamic Testing of Laterally Confined Concrete," in Micromechanics of Failure of Quasi-Brittle Materials, Eds. S. P. Shah, S. E. Swartz and M. L. Wang, Elsevier Applied Science, London and New York, 1990, pp. 343-353.

12. T. Tang, L. E. Malvern, and D. A. Jenkins, "Rate Effects in Uniaxial Dynamic Compression of Concrete," Journal of Engineering Mechanics, Vol. 118, 1992, pp. 108-124.

13. T. Tang, L. E. Malvern, and D. A. Jenkins, "Dynamic Compressive Testing of Concrete and Mortar," Engineering Mechanics in Civil Engineering, eds. A. P. Boresi and K. P. Chong, ASCE, New York, 1984, pp. 663-666.

14. L. E. Malvern, D. A. Jenkins, E. Jerome, and J. C. Gong, Dispersion Correction for split-Hopkinson Pressure Bar Data, Final Report No. ESL-TR-88-04, AFESC, Tyndall AFB, FL, 1987.

15. P. S. Follansbee and C. Frantz, "Wave Propagation in the Split Hopkinson Pressure Bar," Journal of Engineering Materials and Technology, Transactions of the ASME, Vol. 105, 1983, pp. 61-66.

16. C. W. Felice, The Response of Soil to Impulsive Loads Using the Split Hopkinson Pressure Bar Technique, Ph.D. Thesis, University of Utah, Salt Lake City, 1985.

17. H. Tu, Quantitative Characterization of Crack Geometry in Concrete Compressed Uniaxially at High Strain Rate, M.S. Thesis, University of Florida, 1991.

18. C. A. Ross, Crack Patterns Resulting from High Strain-Rate Tests on Concrete, Final Report No. ESL TR 92-08, Air Base Survivability Branch, Engineering Research Division, AFCESA, Tyndall AFB, FL, 1992.

19. R. T. DeHoff and F. N. Rhines, Quantitative Microscopy, McGraw-Hill Book Co., Inc., New York, 1968.

20. E. E. Underwood, Quantitative Stereology, Addison-Wesley Publishing Co., Reading, Mass., 1970.

21. B. Budiansky and R. J. O'Connell, "Elastic Moduli of a Cracked Solid," International Journal of Solids and Structures, Vol. 12, 1976, pp. 81-97.

22. L. M. Taylor, E. P. Chen, and J. S. Kuszmaul, "Microcrack-Induced Damage Accumulation in Brittle Rock under Dynamic

Loading," Computer Methods in Applied Mechanics and Engineering, Vol. 55, (1986), pp. 301-320.

23. M. E. Kipp and D. E. Grady, Numerical Studies of Rock Fragmentation, SAND79-1582, Sandia National Laboratories, Albuquerque, NM, 1978.

24. D. Grady, "The Mechanics of Fracture Under High-Rate Stress Loading," in: Z. P. Bazant, ed., Preprints, William Prager Symposium on Mechanics of Geomaterials: Rocks, Concretes and Soils, Northwestern University, Evanston, IL, 1983, pp. 149-188.

25. M. E. Kipp, D. E. Grady and E. P. Chen, "Strain-rate dependent fracture initiation," International Journal of Fracture, Vol. 17, 1980, pp. 471-478.

26. E. P. Chen, "Continuum Damage Mechanics Studies on the Dynamic Fracture of Concrete," in Cement-Based Composites: Strain Rate Effects on Fracture, Materials Research Society Symposium Proceedings, Vol. 64, eds. S. Mindess and S. P. Shah, Materials Research Society, Pittsburgh, PA, 1986, pp. 63-77.

27. E. P. Chen, "A Continuum Damage Model for the Quasi-static Response of Brittle Materials, in Micromechanics of Failure of Brittle Materials, eds. S. P. Shah, S. E. Swartz, and M. L. Wang, Elsevier Science Publishers, London and New York, 1990, pp. 620-626.

28. E. P. Chen, "A Continuum Damage Model for the Quasistatic Response of a Center-Cracked Plain Concrete Panel in Tension, in Damage Mechanics in Engineering Materials, eds. J. W. Ju, D. Krajcinovic, and H. L. Schreyer, AMD-Vol. 89, MD-Vol. 24, ASME, New York, 1990, pp. 77-87.

29. D. Krajcinovic, "Continuum Damage Mechanics," Applied Mechanics Reviews, Vol. 37, 1984, pp. 1-6.

30. D. Krajcinovic, Reprint of Reference 29, with an update, in Applied Mechanics Update, eds. C. R. Steele and G. S. Springer, ASME, New York, 1986, pp. 397-406.

31. J. W. Ju, D. Krajcinovic, and H. L. Schreyer, eds., Damage Mechanics in Engineering Materials, AMD Vol. 109, MD-Vol. 24, ASME, New York, 1990.

32. V. C. Li, Guest Ed., "Micromechanical modelling of quasi-brittle behavior," in Applied Mechanics Reviews, Vol. 45, no. 8, August 1992, pp 261-398.

33. D. Krajcinovic and G. U. Fonseka, "The Continuous Damage Theory of Brittle Materials, Part 1: General Theory," Journal of Applied Mechanics, Vol. 48, 1981, pp. 809-815.

34. G. U. Fonseka and D. Krajcinovic, "The Continuous Damage Theory of Brittle Materials, Part 2: Uniaxial and Plane Response Modes," Journal of Applied Mechanics, Vol. 48, 1981, pp. 816-824.

35. D. Krajcinovic and S. Selvaraj, "Constitutive Equations for Concrete," in Proc. International Conference on Constitutive Equations for Engineering Materials, Eds. C. S. Desai and R. H. Gallagher, Tucson, Arizona, 1983, pp. 399-406.

36. D. Krajcinovic, "Continuous Damage Mechanics Revisited: Basic Concepts and Definitions," Journal of Applied Mechanics, Vol. 52, 1985, pp. 829-834.

37. D. Krajcinovic and D. Fanella, "A Micromechanical Damage Model for Concrete," Engineering Fracture Mechanics, Vol. 25, 1986, pp. 585-596.

38. D. Fanella and D. Krajcinovic, "A Micromechanical Model for Concrete in Compression," Engineering Fracture Mechanics, Vol. 29, 1988, pp. 49-66.

39. D. Krajcinovic and D. Sumarac, "Micromechanically Based Damage Models," in Proc. 10th US National Congress of Applied Mechanics, J. P. Lamb, ed., ASME, New York, 1987.

40. D. Krajcinovic and D. Sumarac, "A Mesomechanical Model for Brittle Deformation Processes," Journal of Applied Mechanics, Vol. 5, 1989, pp. 51-62.

41. M. Basista, D. Krajcinovic, and D. Sumarac, "Analytical Modeling of the Brittle Deformation of Solids," in Damage Mechanics in Engineering Materials, AMD Vol. 109, MD-Vol. 24, ASME, New York, 1990, pp. 27-39.

42. D. Krajcinovic, M. Basista, and D. Sumarac, "Micro-mechanically Inspired Phenomenological Damage Model," Journal of Applied Mechanics, Vol. 58, 1991, pp. 305-310.

43. J. R. Rice, "Inelastic Constitutive Relations for Solids: an Internal Variable Theory and its Applications to Metal Plasticity," Journal of the Mechanics and Physics of Solids, Vol. 23, 1971, pp. 433-455.

44. H. Horii and S. Nemat-Nasser, "Brittle Failure in Compression: Splitting, Faulting and Brittle-Ductile

Transition," Philosophical Transactions of the Royal Society of London, Vol. A319, 1986, pp. 337-374.

45. M. Kachanov, "Elastic Solids with Many Cracks: a Simple Method of Analysis,"International Journal of Solids and Structures, Vol. 23, 1987, pp. 24-43.

46. J. R. Rice, "Continuum Mechanics and Thermodynamics of Plasticity in Relation to Microscale Deformation Mechanisms," Constitutive Equations in Plasticity, A. S. Argon, ed., MIT Press, Cambridge, Mass., 1975, pp. 23-79.

47. J. W. Rudnicki and J. R. Rice, "Conditions for the Localization of Deformation in Pressure-Sensitive Dilatant Materials," Journal of the Mechanics and Physics of Solids, Vol. 23, 1975, pp. 371-394.

48. S. Nemat-Nasser and M. Obata, "A Microcrack Model of Dilatancy in Brittle Materials, ASME Journal of Applied Mechanics, Vol. 55, 1988, pp. 24-35.

APPENDIX A

CONCRETE PREPARATION AND TREATMENT

Because of the need for opacity and minimal response to UV light, all of the aggregate used was derived from a common stock of Calera limestone supplied by the Civil Engineering Department of the University of Florida. The stock Calera limestone gravel, with maximum size about 3/8 inch, was used directly as the coarse aggregate component, while the fine aggregate consisted of stock material crushed and graded into the proportions shown below:

TABLE A-1. FINE AGGREGATE PROPORTIONS

SIEVE	PARTICLE SIZE(um)	AMOUNT RETAINED		% RETAINED
#4	4760<X	0.0	0.0 gm	0.0%
#8	2380<x<4760	5.7053 lbs	2587.0 gm	12.6%
#16	1190<x<2380	9.5088 lbs	4313.1 gm	21.0%
#30	595<x<1190	11.4106 lbs	5175.7 gm	25.2%
#50	297<x<595	9.5088 lbs	4313.1 gm	21.0%
#100	149<x<297	6.7920 lbs	3080.8 gm	15.0%
Pan	x<149	2.3546 lbs	1068.0 gm	5.2%
Total		45.28 lbs	20538.6 gm	100.0%

TABLE A-2. CONCRETE MIXES

Two separate batches of concrete were prepared as shown below:

BATCH A: November 14, 1990

Type I Portland Cement	18.11 lbs	8241.6 grams
Fine aggregate material	45.28 lbs	20538.6 grams
Calera Limestone aggregate	36.61 lbs	16606.0 grams
Water (Water/Cement ratio .55)	10.00 lbs	4535.9 grams

Measured Slump 1 inch

Total number of molds.....42

BATCH B: November 21, 1990

Type I Portland Cement	18.11 lbs	8241.6 grams
Fine aggregate material	45.28 lbs	20538.6 grams
Calera Limestone aggregate	36.61 lbs	16606.0 grams
Water (Water/Cement ratio .61)	11.00 lbs	4989.5 grams

Measured Slump 2.5 inches

Total number of molds.....40

SPECIMEN INFILTRATION

A quantity of 3M brand 4R Concrete Restorer, a high molecular weight methacrylate system designed for sealing cracks in concrete structures, was generously donated to the project by Mr. George W ost, a Senior Chemist at 3M Corporation in St. Paul, MN. Zyglo Penetrant ZL-22A (Magnaflux Corporation) was used as the source of fluorescent dye. Details of the infiltration procedure are given below.

1. 5 ml of Penetrant ZL-22A are sprayed into a 250 ml plastic beaker.

2. 95 ml of 3M 4R Concrete Restorer (C.R.) component A (Dimethyl Ketone) are added to the beaker and stirred.

3. 3 ml of 3M 4R C.R. component B (Cumene Hydroperoxide) are added to the mixture and stirred.

4. 1 ml of 3M 4R C.R. component C (Cobalt Promoter) is added to the mixture and stirred.

5. After 1 minute, a freshly tested specimen is carefully immersed in the liquid mixture.

6. The loaded beaker is placed in a vacuum chamber and pumped with a small mechanical pump for 15 to 20 minutes.

7. After removal from the vacuum chamber, the mixture hardens in 2 to 3 hours and is allowed to cure for at least one week before sectioning with a diamond saw.

APPENDIX B
TEST RESULTS

1. STATIC TEST RESULTS

LABEL Batch-A	STRAIN (%)	LA 1/mm	END/A 1/mm^2	BRAN/A 1/mm^2	ORIENT
A-15-2	0.22	0.090	0.142	0.043	0.182
A-16-2	0.25	0.163	0.166	0.075	0.249
A-17-2	0.28	0.132	0.156	0.052	0.352
A-18-2	0.31	0.109	0.138	0.037	0.237
A-19-2	0.34	0.185	0.220	0.080	0.171
A-20-2	0.38	0.389	0.310	0.168	0.251
A-21-2	0.40	0.248	0.207	0.080	0.298
A-22-2	0.44	0.472	0.300	0.195	0.229
A-23-2	0.46	0.402	0.310	0.164	0.252
A-24-2	0.49	0.120	0.131	0.044	0.293
A-25-2	0.54	0.644	0.433	0.267	240
A-26-2	0.55	0.651	0.471	0.342	0.142
A-27-2	0.58	0.252	0.218	0.085	0.260
A-28-2	0.62	0.632	0.422	0.302	0.180

LABEL Batch-B	STRAIN (%)	LA 1/mm	END/A 1/mm^2	BRAN/A 1/mm^2	ORIENT
B-12-1	0.13	0.110	0.103	0.046	0.178
B-13-1	0.15	0.091	0.091	0.034	0.158
B-15-1	0.22	0.110	0.091	0.057	0.212
B-16-1	0.25	0.301	0.210	0.151	0.169
B-17-1	0.28	0.378	0.199	0.175	0.169
B-19-1	0.34	0.090	0.087	0.032	0.240
B-21-1	0.40	0.442	0.272	0.172	0.190
B-22-1	0.45	0.616	0.300	0.259	0.210
B-23-1	0.46	0.700	0.357	0.251	0.211
B-24-1	0.51	0.803	0.327	0.339	0.173
B-25-1	0.52	0.617	0.321	0.229	0.209
B-26-1	0.57	0.952	0.381	0.354	0.171
B-27-1	0.60	0.732	0.331	0.278	0.216
B-28-1	0.61	0.727	0.367	0.291	0.206

2. DYNAMIC TEST RESULTS

LABEL Batch-A	STRAIN (%)	LA 1/mm	END/A 1/mm^2	BRAN/A 1/mm^2	ORIENT
A-01-01	0.09	0.035	0.045	0.029	0.094
A-02-01	0.09	0.104	0.100	0.053	0.140
A-03-01	0.22	0.274	0.166	0.125	0.107
A-04-01	0.13	0.149	0.095	0.071	0.108
A-05-01	0.17	0.093	0.103	0.044	0.078
A-06-01		0.217	0.158	0.104	0.062
A-07-01	0.15	0.387	0.201	0.177	0.086
A-08-01	0.24	0.456	0.337	0.180	0.242
A-09-01	0.30	0.555	0.313	0.242	0.125
A-10-01	0.32	0.588	0.421	0.246	0.175
A-11-01	0.34	0.536	0.371	0.244	0.148
A-12-01	0.36	0.919	0.453	0.460	0.119
A-13-01	0.39	0.838	0.377	0.452	0.077
A-14-01	0.42	0.774	0.398	0.374	0.148
A-15-01	0.45	1.155	0.640	0.591	0.102
A-17-01	0.48	1.160	0.578	0.646	0.095
A-18-01	0.55	1.163	.575	0.692	0.084
A-19-01	0.57	1.215	.723	0.757	0.094
A-20-01	0.61	1.424	0.597	0.972	0.070
A-21-01		1.506	0.703	1.125	0.043
A-22-01	0.61	1.293	0.449	0.854	0.077
A-23-01	0.67	1.562	0.539	1.157	0.056
A-24-01	0.63	1.483	0.474	0.947	0.090
A-25-01	0.64	1.498	0.552	1.062	0.104
A-26-01	0.78	1.479	0.400	0.948	0.104
A-28-01	0.84	1.362	0.496	0.787	0.147

2. DYNAMIC TEST RESULTS (cont.)

LABEL Batch-B	STRAIN (%)	LA 1/mm	END/A 1/mm^2	BRAN/A 1/mm^2	ORIENT
B-01-2	0.12	0.063	0.070	0.024	0.024
B-02-2	0.22	0.380	0.173	0.143	0.098
B-03-2	0.08	0.300	0.129	0.117	0.085
B-05-2	0.18	0.164	0.105	0.057	0.092
B-07-2	0.20	0.508	0.174	0.186	03062
B-09-2	0.24	0.809	0.257	0.354	0.083
B-10-2	0.29	1.068	0.348	0.512	0.076
B-13-2	0.41	1.590	0.524	0.956	0.057
B-14-2	0.23	1.325	0.409	0.607	0.081
B-15-2	0.45	1.599	0.374	0.855	0.073
B-16-2	0.49	1.687	0.344	0.926	0.063
B-17-2	0.56	1.676	0.445	0.977	0.096
B-18-2	0.56	1.617	0.378	0.848	0.051
B-19-2	0.57	1.800	0.464	1.126	0.054
B-20-2	0.68	1.646	0.380	0.949	0.070
B-21-2	0.62	1.557	0.341	0.843	0.069
B-22-2	0.63	1.833	0.602	1.350	0.085
B-24-2	0.76	1.936	0.473	1.369	0.081
B-25-2	0.80	1.452	0.424	0.989	0.108
B-27-2	0.81	1.740	0.416	1.181	0.057
B-28-2	0.82	1.774	0.482	1.149	0.098